Computer Methods in Applied Mechanics and Engineering 441 (2025) 117949

Contents lists available at ScienceDirect

Comput. Methods Appl. Mech. Engrg.

journal homepage: www.elsevier.com/locate/cma

Stress-constrained versus fracture-based topology optimization: A comparative study

Yingqi Jia [a], Rahul Dev Kundu [a], Xiaojia Shelly Zhang [a,b,c,*]

[a] *Department of Civil and Environmental Engineering, University of Illinois Urbana-Champaign, Urbana, IL 61801, USA*
[b] *Department of Mechanical Science and Engineering, University of Illinois Urbana-Champaign, Urbana, IL 61801, USA*
[c] *National Center for Supercomputing Applications, Urbana, IL 61801, USA*

ARTICLE INFO

Keywords:
Topology optimization
Fracture
Stress constraint
Strength surface
Phase field
Critical energy release rate
Toughness

ABSTRACT

Stress-constrained and fracture-based topology optimization are both popular methods to enhance fracture resistance in engineering structures and materials. However, their comparative advantages and applicability to various design scenarios remain underexplored. In this study, we revisit both formulations and systematically compare them by analyzing their underlying physics and capabilities. The stress-constrained formulation incorporates material strength surfaces as constraints, while the fracture-based formulation models both crack nucleation and propagation using a strongly coupled phase-field fracture theory. We then assess their optimized structures across several benchmark design scenarios accounting for various fracture behaviors. Our comparisons reveal several key insights. First, both formulations perform equivalently in design domains under uniform stress states, where the strength surface governs fracture nucleation. Second, the fracture-based formulation consistently produces feasible solutions in design domains with boundary defects and large pre-cracks, where the critical energy release rate becomes crucial in fracture nucleation. In this scenario, the stress-constrained formulation operates by eliminating stress concentrations; however, it may underestimate the fracture resistance of a structure due to the lack of information on the critical energy release rate. Third, the fracture-based formulation is preferable when the design priority is structural toughness maximization that involves both fracture nucleation and propagation. Finally, despite some limitations in the design performance, the stress-constrained formulation offers better computational efficiency and simpler implementation. These findings shed light on the similarities and differences between the two formulations and provide guidelines for selecting the suitable approach for practical design problems.

1. Introduction

Fractures are pervasive in materials and structures, making it crucial to enhance fracture resistance in engineering applications to ensure safety and minimize economic loss. Traditional methods [1,2] for improving structural fracture resistance often rely on the designer's experience and intuition, therefore these approaches may not fully exploit a material's potential. It calls for a more rigorous mechanics-based and optimization-driven design approach.

To generate optimal structural designs, topology optimization [3–5] has been widely utilized across various fields, including civil [6,7], mechanical [8–10], aerospace [11], and biological [12,13] engineering. This design methodology seeks the optimal

* Corresponding author at: Department of Civil and Environmental Engineering, University of Illinois Urbana-Champaign, Urbana, IL 61801, USA.
E-mail address: zhangxs@illinois.edu (X.S. Zhang).

https://doi.org/10.1016/j.cma.2025.117949
Received 5 November 2024; Received in revised form 17 March 2025; Accepted 18 March 2025
Available online 9 April 2025

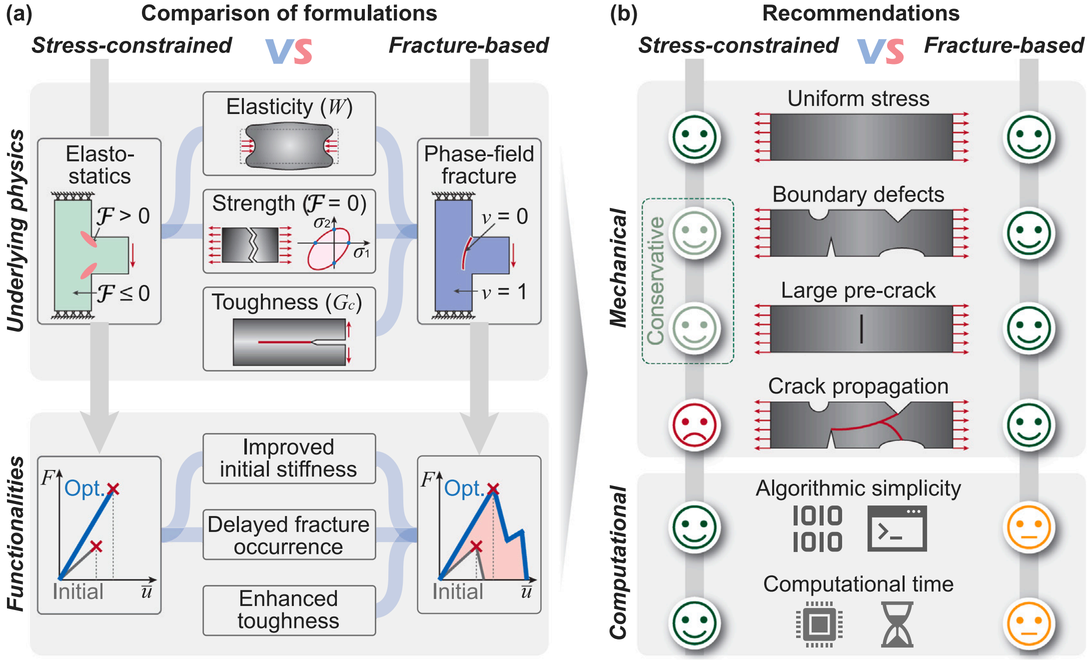

Fig. 1. Comparison between the stress-constrained and fracture-based topology optimization. (a) Comparison of the two formulations. The material parameters W, $\mathcal{F}$, and G_c are the strain energy density, strength surface function, and critical energy release rate, respectively. The variables σ_1 and σ_2 are the principal stresses. The condition $\mathcal{F} \leq 0$ represents that the stress state is within or on the strength surface, while $\mathcal{F} > 0$ signifies a violation of the strength surface. The variable v is the phase field with $v = 1$ representing intact material and $v = 0$ representing fractured material. The variables F and $\bar{u}$ are the resultant reaction force and the amplitude of the applied displacement, respectively. (b) Recommendations for applying the two formulations based on various mechanical and computational criteria.

material layout by maximizing or minimizing a given objective function while adhering to prescribed constraints. The extensive design space, precise modeling of underlying physics, and the use of gradient-based optimizers make topology optimization a superior candidate for enhancing fracture resistance, and significant advancements [7,14–18] have been made in this area recently.

Within the domain of topology optimization for enhancing fracture resistance, two prominent approaches have emerged: stress-constrained and fracture-based formulations. The stress-constrained formulation limits the stress states (e.g., the von Mises stress and the first principal stress) within the material's strength surface [16,19–23]. By dispersing high local stress concentrations through optimized topology and/or geometry, the stress-constrained formulation is generally effective in delaying fracture nucleation. In the small-strain linear elastic regime, this approach requires only the stress computation from the solved displacement field, without the need to simulate post-failure scenarios (i.e., fracture [7,24] and plasticity [25,26]). Because of its simplicity, the stress-constrained formulation has been extensively explored and has demonstrated considerable success [19,27–36] with applications in designing multiscale and infill structures [37–39], developing multimaterial structures [40,41], enhancing fatigue life [42,43], and improving structural reliability [44].

Fracture-based formulations [7,24,45–54] have also gained increasing attention. These formulations are typically grounded in the phase-field regularization [55,56] of the variational theory of brittle fracture [57], corresponding to Griffith's competition [58] between the strain and fracture energies. This phase-field fracture theory, as will be shown in Tables 2–3, predicts fracture nucleation consistent with the strength theory for specimens under uniform stress and aligns with linear elastic fracture mechanics (LEFM) for cracked specimens. By incorporating phase-field fracture modeling, the fracture-based formulations can directly predict and control fracture responses without explicitly including the stress constraints.

Despite the widespread use of both stress-constrained and fracture-based formulations, their comparative advantages and applicability to various design scenarios remain unclear. Specifically, two long-standing questions arise:

(i) *Is the stress-constrained formulation sufficient for optimizing fracture-resistant structures in all design scenarios without explicitly accounting for fracture mechanics?*
(ii) *What justifies the use of the more complex and computationally expensive fracture-based formulation?*

These questions remain open largely because of the lack of a systematic comparison between the two formulations. Recently, a fracture-based formulation in [7] integrated a phase-field fracture theory [56] that can predict fracture nucleation by implicitly incorporating a strength surface comparable with the strength theory, forming the basis for a rigorous comparison with the stress-based formulation. Thus, in this study, we conduct a systematic and quantitative comparison of the underlying physics and functionalities of stress-constrained and fracture-based topology optimization (Fig. 1(a)). By comparing these two design approaches for improving brittle fracture resistance of structures in the same set of design problems, we aim to answer the two aforementioned questions, reveal the similarities and differences between the two formulations, and shed light on *when* and *why* one formulation should be favored over the other for a given design task.

To ensure a representative comparison, we employ state-of-the-art versions of both formulations. The stress-constrained formulation has multiple variants, including global aggregation [22,59] and its reformulation [60], single-domain integration [61], a plasticity-inspired method [62], machine learning-enhanced stress calculation [63,64], active and loss functions [65], and the augmented Lagrangian (AL) approach [21,28,66]. In this study, we use a stress-constrained formulation equipped with the AL scheme. This scheme maintains the localized nature of stress constraints while efficiently managing a large number of them [67], which has been shown to have overall better efficiency and performance for medium- to large-scale problems compared to global aggregation methods [22]. Essentially, the employed stress-constrained formulation predicts stress states within the design domain using elastostatics based on elasticity information (strain energy density, W) and precisely limits local stress within a given material strength surface ($\mathcal{F} = 0$). Consequently, the stress-constrained approach can delay the onset of fracture compared to empirical designs. In general, without additional design considerations (e.g., fail-safe strategies [68–70]), the stress-constrained formulations do not incorporate any information on the structural response after the onset of fracture, and therefore is not designed for enhancing overall effective toughness of structures.

For the fracture-based formulation (Fig. 1(a)), we adopt a multi-objective approach from [7]. This formulation is based on a comprehensive phase-field fracture theory [56], which incorporates elasticity (W), the strength surface ($\mathcal{F} = 0$), and the critical energy release rate (G_c) to accurately predict both the nucleation and propagation of brittle fractures, as validated in various experiments [56,71,72]. As a result, this fracture-based approach not only delays fracture onset and improves the initial stiffness but also enhances the overall effective toughness of structures.

By comparing stress-constrained and fracture-based topology optimization, we provide insights into their similarities and differences and offer recommendations for specific optimization tasks considering both mechanical and computational aspects. As shown in Fig. 1(b), for structures subjected to uniform stress states where the strength surface ($\mathcal{F} = 0$) governs the fracture nucleation, both formulations yield equivalent design performance. However, for structures with boundary defects (such as rounded or sharp corners) and/or large pre-existing cracks, the critical energy release rate (G_c) becomes essential for accurately predicting fracture nucleation [56], making the fracture-based formulation more comprehensive for optimizing fracture-resistant designs. In these scenarios, the stress-constrained formulation is generally effective in delaying fracture nucleation by identifying stress concentrations. However, it tends to be more conservative in estimating failure displacements due to the absence of G_c information, and consequently, it may struggle to converge with a given allowable volume fraction when the target failure displacement is excessively large. Finally, when crack propagation is a critical factor, the fracture-based formulation is preferable because of its incorporation of G_c into the optimization process. Nevertheless, from a computational standpoint, the stress-constrained formulation demonstrates greater efficiency due to simpler computational methods and shorter runtime, making it preferable for large-scale structural optimization tasks.

In the remainder of this study, we further explain the above comparisons and recommendations, and the organization of the study is as follows: Section 2 introduces the elastostatics and phase-field fracture theory, which serve as state equations in the topology optimization formulations recapped in Section 3. Next, Section 4 systematically compares the stress-constrained and fracture-based formulations through three groups of representative examples. Finally, Section 5 presents several concluding remarks. The paper includes four appendices. Appendix A derives the critical applied traction for cracked specimens using the strength criterion. Appendix B presents the computer algorithms for the stress-constrained and fracture-based topology optimization formulations for reproducibility. Appendix C discusses stiffness maximization of structures under displacement loading. Lastly, Appendix D details the computational time for both formulations across all examples in Section 4.

2. Elastostatics and phase-field fracture theory

In this section, we recap the elastostatics [73] and phase-field fracture theory [56,71] under small deformations. These theories provide the state equations used in the topology optimization formulations discussed in Section 3.

2.1. Elastostatics

We begin by introducing the governing equations of the elastostatics. For an open-bounded design domain (Ω) with boundary $\partial\Omega$, the displacement field ($\mathbf{u}(\mathbf{X})$) of any given material point, $\mathbf{X} \in \overline{\Omega} = \Omega \cup \partial\Omega$, is governed by

$$\begin{cases} \mathrm{Div}\left[\dfrac{\partial W}{\partial \mathbf{E}}(\mathbf{E}(\mathbf{u}))\right] + \overline{\mathbf{b}}(\mathbf{X}) = \mathbf{0}, & \mathbf{X} \in \Omega \\ \mathbf{u}(\mathbf{X}) = \overline{\mathbf{u}}(\mathbf{X}), & \mathbf{X} \in \partial\Omega_{\mathcal{D}} \\ \left[\dfrac{\partial W}{\partial \mathbf{E}}(\mathbf{E}(\mathbf{u}))\right]\mathbf{N} = \overline{\mathbf{t}}(\mathbf{X}), & \mathbf{X} \in \partial\Omega_{\mathcal{N}}. \end{cases} \tag{1}$$

Here, the variable W is the stored energy function defined as

$$W(\mathbf{E}(\mathbf{u})) = \mu \mathrm{tr}\left[\mathbf{E}^2(\mathbf{u})\right] + \frac{\lambda}{2}\mathrm{tr}^2\left[\mathbf{E}(\mathbf{u})\right]$$

where λ and μ are the first and second Lamé constants, respectively. The variable $\mathbf{E}(\mathbf{u}) = \left[\nabla\mathbf{u} + (\nabla\mathbf{u})^{\mathsf{T}}\right]/2$ is the infinitesimal strain tensor. The variables $\overline{\mathbf{b}}$, $\overline{\mathbf{t}}$, and $\overline{\mathbf{u}}$ are the prescribed body force, traction, and displacement, respectively. The symbols $\partial\Omega_{D}$ and $\partial\Omega_{\mathcal{N}}$ are the Dirichlet and Neumann boundaries, respectively, and $\mathbf{N}$ is the unit outward normal vector of $\partial\Omega$.

2.2. Phase-field fracture theory

2.2.1. Governing equations

After introducing the classical elastostatics, we generalize it to the phase-field fracture theory [56,71]. In addition to the displacement field ($\mathbf{u}(\mathbf{X})$) defined above, we introduce a dimensionless phase field or an order parameter, $v(\mathbf{X}) \in [0,1]$, to describe the damage of materials. Precisely, $v(\mathbf{X}) = 1$ corresponds to the intact material, whereas $v(\mathbf{X}) = 0$ represents the fractured material.

For a discretized time interval, $\{0 = t_0, t_1, \ldots, t_k, t_{k+1}, \ldots, t_{N-1}, t_N = T\}$, the displacement field ($\mathbf{u}_k(\mathbf{X}) = \mathbf{u}(\mathbf{X}, t_k)$) and phase field ($v_k(\mathbf{X}) = v(\mathbf{X}, t_k)$) at time t_k are controlled by a system of strongly coupled partial differential equations (PDEs) expressed as [56,71]

$$\begin{cases} \mathrm{Div}\left[v_k^2 \dfrac{\partial W}{\partial \mathbf{E}}(\mathbf{E}(\mathbf{u}_k))\right] + \overline{\mathbf{b}}_k(\mathbf{X}) = \mathbf{0}, & \mathbf{X} \in \Omega \\ \mathbf{u}_k(\mathbf{X}) = \overline{\mathbf{u}}_k(\mathbf{X}), & \mathbf{X} \in \partial\Omega_D \\ \left[v_k^2 \dfrac{\partial W}{\partial \mathbf{E}}(\mathbf{E}(\mathbf{u}_k))\right]\mathbf{N} = \overline{\mathbf{t}}_k(\mathbf{X}), & \mathbf{X} \in \partial\Omega_{\mathcal{N}} \end{cases} \tag{2}$$

and

$$\begin{cases} \mathrm{Div}[\varepsilon\delta^{\varepsilon} G_c \nabla v_k] = \dfrac{8}{3} v_k W(\mathbf{E}(\mathbf{u}_k)) - \dfrac{4}{3} c_{\mathrm{e},k} - \dfrac{\delta^{\varepsilon} G_c}{2\varepsilon} + \dfrac{4}{3}\dfrac{\partial W_v(v_k, v_{k-1})}{\partial v_k}, & \mathbf{X} \in \Omega \\ \nabla v_k \cdot \mathbf{N} = 0, & \mathbf{X} \in \partial\Omega \end{cases} \tag{3}$$

with $\mathbf{u}_0(\mathbf{X}) \equiv \mathbf{0}$ and $v_0(\mathbf{X}) \equiv 1$.

In these equations, we let $\overline{\mathbf{b}}_k(\mathbf{X}) = \overline{\mathbf{b}}(\mathbf{X}, t_k)$, $\overline{\mathbf{t}}_k(\mathbf{X}) = \overline{\mathbf{t}}(\mathbf{X}, t_k)$, and $\overline{\mathbf{u}}_k(\mathbf{X}) = \overline{\mathbf{u}}(\mathbf{X}, t_k)$. The material constant G_c is the critical energy release rate. The parameter $\varepsilon > 0$ is a regularization (or localization) length, and δ^{ε} is a dimensionless and ε-dependent parameter given as [74,75]

$$\delta^{\varepsilon} = \left(1 + \frac{3h}{8\varepsilon}\right)^{-2} \frac{(5 + 4\sqrt{3})\sigma_{\mathtt{cs}} - 3\sigma_{\mathtt{ts}}}{2(8 + 3\sqrt{3})\sigma_{\mathtt{cs}}} \frac{3G_c}{16\mathcal{W}_{\mathtt{ts}}\varepsilon} + \left(1 + \frac{3h}{8\varepsilon}\right)^{-1} \frac{2}{5}.$$

The parameters $\sigma_{\mathtt{ts}}$ and $\sigma_{\mathtt{cs}}$ are the uniaxial tensile and compressive strengths, respectively. The parameter $\mathcal{W}_{\mathtt{ts}}$ is the critical strain energy density under uniaxial tensile loading when fracture nucleates. Under infinitesimal deformation, it reads as $\mathcal{W}_{\mathtt{ts}} = \sigma_{\mathtt{ts}}^2/2E$ with E representing the Young's modulus of the materials. The parameter h represents the element size in the standard finite element analysis (FEA), and $1 + 3h/8\varepsilon$ is the correction term.

The variable $W_v(v_k, v_{k-1})$ in (3)$_1$ is an energy-like penalty term defined as [76]

$$W_v(v_k, v_{k-1}) = \frac{p_v}{2}\left\{(|v_k| - v_k)^2 + [|v_{k-1} - v_k| - (v_{k-1} - v_k)]^2\right\}$$

with a coefficient

$$p_v = 10^3 \max\{\delta^{\varepsilon}, 1\}\frac{3G_c}{8\varepsilon}, \tag{4}$$

which imposes the inequality constraints of $0 \le v_k \le v_{k-1} \le 1$ for fracture irreversibility. Based on Section 4.1 of [76], the coefficient p_v needs to satisfy $p_v \gg G_c/\varepsilon$ to effectively enforce the inequality constraints on v_k. The expression for p_v in (4) follows the choice made in [76] and its corresponding open-source implementation.[1] This selection of p_v generally ensures that the phase field solutions (v_k) conform to the inequality constraints with a precision of $\mathcal{O}(10^{-3})$. Finally, Eqs. (2)–(3) are fully explicit except for the external driving force, $c_{\mathrm{e},k}(\mathbf{X}) = c_{\mathrm{e}}(\mathbf{X}, t_k)$, which is introduced in Section 2.2.2 below.

Remark 1. The Euler–Lagrange equations in (2)–(3) reduce to the classical phase-field fracture theory [55] by setting $\delta^{\varepsilon} \equiv 1$ and $c_{\mathrm{e},k} \equiv 0$, and the latter is derived by minimizing of the potential energy expressed as

$$\begin{aligned} \mathcal{E}^{\varepsilon}(\mathbf{u}_k, v_k; v_{k-1}) &= \int_{\Omega} v_k^2\, W(\mathbf{E}(\mathbf{u}_k))\mathrm{d}\mathbf{X} + \int_{\Omega} \frac{3G_c}{8}\left(\frac{1 - v_k}{\varepsilon} + \varepsilon\nabla v_k \cdot \nabla v_k\right)\mathrm{d}\mathbf{X} + \int_{\Omega} W_v(v_k, v_{k-1})\mathrm{d}\mathbf{X} \\ &\quad - \int_{\Omega} \overline{\mathbf{b}}_k \cdot \mathbf{u}_k \mathrm{d}\mathbf{X} - \int_{\partial\Omega_{\mathcal{N}}} \overline{\mathbf{t}}_k \cdot \mathbf{u}_k \mathrm{d}\mathbf{X} \end{aligned}$$

subject to $\mathbf{u}_k = \overline{\mathbf{u}}_k$ on $\partial\Omega_D$. Here, the first three terms are the strain, fracture, and penalty energies, respectively, and the last two terms are the work done by $\overline{\mathbf{b}}_k$ and $\overline{\mathbf{t}}_k$. By further setting $v_k \equiv 1$ (no fracture occurrence), the equations in (2)–(3) reduce to the elastostatic ones in (1).

[1] The open-source code is available at https://github.com/farhadkama/FEniCSx_Kamarei_Kumar_Lopez-Pamies.

Table 1
Fracture-related parameters of tested brittle materials.

Parameters	Borosilicate glass [71]	Graphite [56]	Titania [56]	PMMA [71]	Artificial [7]
E (GPa)	80.00	9.80	97.00	5.05	0.98
ν	0.22	0.13	0.29	0.40	0.13
G_c (N/m)	9	91	36	480	910
σ_{ts} (MPa)	150	27	100	128	27
σ_{cs} (MPa)	1000	77	1232	256	77
ε (μm)	1	20	5	2	20

2.2.2. External driving force

In this section, we introduce the external driving force ($c_{\mathrm{e},k}$) that appears in (3)$_1$. This $c_{\mathrm{e},k}$ term is designed such that Eqs. (2)–(3) predict fracture nucleation from the body of Ω under uniform state stress according to the material strength surface. In this study, we opt to use the Drucker–Prager strength surface [77] expressed as

$$\mathcal{F}(I_1,J_2)=\sqrt{J_2}+\frac{\sigma_{\mathrm{cs}}-\sigma_{\mathrm{ts}}}{\sqrt{3}(\sigma_{\mathrm{cs}}+\sigma_{\mathrm{ts}})}I_1-\frac{2\sigma_{\mathrm{cs}}\sigma_{\mathrm{ts}}}{\sqrt{3}(\sigma_{\mathrm{cs}}+\sigma_{\mathrm{ts}})}=0, \tag{5}$$

which accurately predicts brittle fracture of materials [56,78]. The stress invariants I_1 and J_2 are defined as

$$I_1=\mathrm{tr}(\boldsymbol{\sigma})=(3\lambda+2\mu)\mathrm{tr}[\mathbf{E}(\mathbf{u})] \quad \text{and} \quad J_2=\frac{1}{2}\mathrm{tr}(\boldsymbol{\sigma}_D^2)=2\mu^2\mathrm{tr}[\mathbf{E}_D^2(\mathbf{u})]$$

with

$$\boldsymbol{\sigma}_D=\boldsymbol{\sigma}-\frac{1}{3}\mathrm{tr}(\boldsymbol{\sigma})\mathbf{I} \quad \text{and} \quad \mathbf{E}_D=\mathbf{E}-\frac{1}{3}\mathrm{tr}(\mathbf{E})\mathbf{I}.$$

Here, the variable $\boldsymbol{\sigma}$ is the infinitesimal stress tensor computed as

$$\boldsymbol{\sigma}(\mathbf{E}(\mathbf{u}))=\frac{\partial W}{\partial \mathbf{E}}(\mathbf{E}(\mathbf{u}))=2\mu\mathbf{E}(\mathbf{u})+\lambda\mathrm{tr}[\mathbf{E}(\mathbf{u})]\mathbf{I}.$$

For the material strength surface given in (5), we define the external driving force as

$$\begin{aligned} c_{\mathrm{e},k}(I_1,J_2;v_k;\varepsilon)= \quad & -\left[\frac{\sqrt{3}\delta^{\varepsilon}(\sigma_{\mathrm{cs}}+\sigma_{\mathrm{ts}})}{2\sigma_{\mathrm{cs}}\sigma_{\mathrm{ts}}}\frac{3G_c}{8\varepsilon}+\frac{\sqrt{3}\mathcal{W}_{\mathrm{ts}}}{\sigma_{\mathrm{ts}}}\right]v_k^2\sqrt{J_2}-\left[\frac{\delta^{\varepsilon}(\sigma_{\mathrm{cs}}-\sigma_{\mathrm{ts}})}{2\sigma_{\mathrm{cs}}\sigma_{\mathrm{ts}}}\frac{3G_c}{8\varepsilon}+\frac{\mathcal{W}_{\mathrm{ts}}}{\sigma_{\mathrm{ts}}}\right]v_k^2 I_1 \\ & +v_k[1-\mathrm{sgn}(I_1)]\left[\frac{J_2}{2\mu}+\frac{I_1^2}{6(3\lambda+2\mu)}\right]. \end{aligned} \tag{6}$$

Based on strongly coupled PDEs in (2)–(3) along with the external driving force in (6), we derive a fully explicit and complete phase-field fracture theory. The detailed computational procedure is outlined in Algorithm 3. In the next section, we will compare it with the classical strength theory based on (5).

2.3. Phase-field fracture theory versus strength theory

In this section, we compare the phase-field fracture theory and the strength theory — that will be used later as state equations in the topology optimization formulations discussed in Section 3 — on two representative mechanical domains: under uniform stress states and with large and sharp pre-cracks. For both scenarios, we test a broad spectrum of brittle materials shown in Table 1. The analyses and the test results are as follows.

2.3.1. Mechanical domains with uniform stress states

We begin by considering the mechanical domains with uniform stress states. In this case, we can show that the governing equations in (2)–(3) predicts an ε-dependent strength surface expressed as [56]

$$\mathcal{F}^{\varepsilon}(I_1,J_2;\varepsilon)=\frac{J_2}{\mu}+\frac{I_1^2}{3(3\lambda+2\mu)}-c_{\mathrm{e},k}(I_1,J_2;v_k\equiv 1;\varepsilon)-\frac{3\delta^{\varepsilon}G_c}{8\varepsilon}=0.$$

With the choice of $c_{\mathrm{e},k}$ in (6), the predicted strength surface can be rewritten as

$$\begin{aligned} \mathcal{F}^{\varepsilon}(I_1,J_2;\varepsilon)= \quad & \frac{3\sqrt{3}\delta^{\varepsilon}(\sigma_{\mathrm{cs}}+\sigma_{\mathrm{ts}})G_c}{16\varepsilon\sigma_{\mathrm{cs}}\sigma_{\mathrm{ts}}}\left[\sqrt{J_2}+\frac{\sigma_{\mathrm{cs}}-\sigma_{\mathrm{ts}}}{\sqrt{3}(\sigma_{\mathrm{cs}}+\sigma_{\mathrm{ts}})}I_1-\frac{2\sigma_{\mathrm{cs}}\sigma_{\mathrm{ts}}}{\sqrt{3}(\sigma_{\mathrm{cs}}+\sigma_{\mathrm{ts}})}\right] \\ & +\frac{\sqrt{3}\mathcal{W}_{\mathrm{ts}}}{\sigma_{\mathrm{ts}}}\sqrt{J_2}+\frac{\mathcal{W}_{\mathrm{ts}}}{\sigma_{\mathrm{ts}}}I_1+[1+\mathrm{sgn}(I_1)]\left[\frac{J_2}{2\mu}+\frac{I_1^2}{6(3\lambda+2\mu)}\right]. \end{aligned} \tag{7}$$

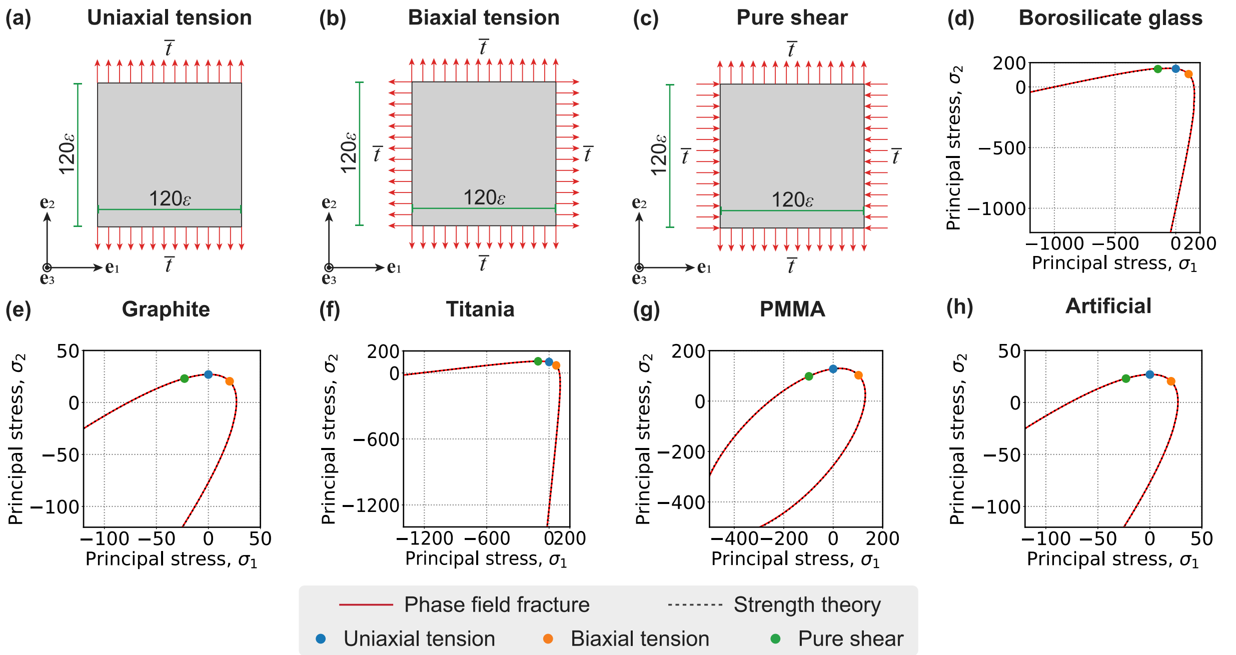

Fig. 2. Comparison between phase-field fracture and strength theories for mechanical domains under uniform stress states. (a)–(c) Three tested mechanical domains under uniaxial tension, biaxial tension, and pure shear, respectively. (d)–(h) Strength surfaces of the borosilicate glass, graphite, titania, PMMA, and artificial materials, respectively. The solid line represents the strength surface ($\mathcal{F}^\varepsilon = 0$) predicted by the phase-field fracture theory in (2)–(3). The dashed line represents the strength surface ($\mathcal{F} = 0$) of the strength theory in (5). The circular dots demonstrate the failure states predicted by the phase-field fracture theory.

Remark 2. The Euler–Lagrange equations in (2)–(3) can now be interpreted as follows. Mathematically, when I_1 and J_2 increase from zeros until $\mathcal{F}^\varepsilon(I_1, J_2; \varepsilon) = 0$, the PDE in (3) becomes unstable. At this point, the variable v_k bifurcates from being identically 1 to a heterogeneous solution where v_k decreases locally [56]. Mechanically, the equations in (2)–(3) implicitly define a strength surface given by $\mathcal{F}^\varepsilon(I_1, J_2; \varepsilon) = 0$. Fracture nucleation occurs when the stress state (I_1, J_2) reaches this surface, leading to a localized decrease in the phase-field variable v_k, which further induces damage in the material elasticity by downscaling the strain energy density (W) with v_k^2 in (2).

Remark 3. As $\varepsilon \searrow 0$, the strength surface predicted by (2)–(3) is reduced to

$$\hat{\mathcal{F}}^\varepsilon(I_1, J_2; \varepsilon) = \frac{3\sqrt{3}\delta^\varepsilon(\sigma_{\mathrm{cs}} + \sigma_{\mathrm{ts}})G_c}{16\varepsilon\sigma_{\mathrm{cs}}\sigma_{\mathrm{ts}}}\left[\sqrt{J_2} + \frac{\sigma_{\mathrm{cs}} - \sigma_{\mathrm{ts}}}{\sqrt{3}(\sigma_{\mathrm{cs}} + \sigma_{\mathrm{ts}})}I_1 - \frac{2\sigma_{\mathrm{cs}}\sigma_{\mathrm{ts}}}{\sqrt{3}(\sigma_{\mathrm{cs}} + \sigma_{\mathrm{ts}})}\right] = 0,$$

which predicts the fracture nucleation the same as the classical strength theory in (5).

Remark 4. For finite values of $\varepsilon > 0$, the strength surface in (7) accurately predicts the fracture nucleation under the uniaxial tensile ($I_1 = \sigma_{\mathrm{ts}}$ and $J_2 = \sigma_{\mathrm{ts}}^2/3$) and compressive ($I_1 = -\sigma_{\mathrm{cs}}$ and $J_2 = \sigma_{\mathrm{cs}}^2/3$) loadings. This can be proved by examining $\mathcal{F}^\varepsilon(\sigma_{\mathrm{ts}}, \sigma_{\mathrm{ts}}^2/3; \varepsilon) = \mathcal{F}^\varepsilon(-\sigma_{\mathrm{cs}}, \sigma_{\mathrm{cs}}^2/3; \varepsilon) = 0$.

We now compare the phase-field fracture and strength theories using numerical examples. As illustrated in Fig. 2(a)–(c), we analyze a square domain under three representative types of uniform stress states within a plane stress condition: uniaxial tension ($\sigma_2 = \bar{t}$ and $\sigma_1 = \sigma_3 = 0$), biaxial tension ($\sigma_1 = \sigma_2 = \bar{t}$ and $\sigma_3 = 0$), and pure shear ($\sigma_2 = -\sigma_1 = \bar{t}$ and $\sigma_3 = 0$). Here, σ_1, σ_2, and σ_3 denote the principal stresses, and $\bar{t} = |\bar{\mathbf{t}}|$ represents the amplitude of the applied traction.

Based on these setups, we examine the strength surfaces of the phase-field fracture theory in (7) and the strength theory in (5) for the five brittle materials in Table 1. As shown in Fig. 2(d)–(h), the strength surfaces derived from both theories exhibit agreement for all five materials as expected. Additionally, to enhance understanding of the setups in Fig. 2(a)–(c), we present the failure stress states for each material as predicted by the phase-field fracture theory using FEA.

To enable a quantitative comparison, we compute the critical applied tractions of the phase-field fracture ($\bar{t}_{\mathrm{cr}}^{\mathrm{PF}}$) and strength ($\bar{t}_{\mathrm{cr}}^{\mathcal{F}}$) theories. The former is derived through a standard FEA with an element size of $h = \varepsilon/5$ for each material, while the latter can be

Table 2
Critical applied tractions under uniform stress states (unit: MPa).

Load cases	Failure criteria	Borosilicate glass	Graphite	Titania	PMMA	Artificial
Uniaxial tension	Strength theory ($\bar{t}_{cr}^{\mathcal{F}}$)	150.00	27.00	100.00	128.00	27.00
	Phase-field fracture ($\bar{t}_{cr}^{PF}$)	149.40	26.89	99.60	127.48	26.89
		(−0.40%)	(−0.40%)	(−0.40%)	(−0.40%)	(−0.40%)
Biaxial tension	Strength theory ($\bar{t}_{cr}^{\mathcal{F}}$)	105.26	20.38	68.52	102.40	20.38
	Phase-field fracture ($\bar{t}_{cr}^{PF}$)	105.74	20.40	68.61	102.49	20.40
		(0.45%)	(0.07%)	(0.14%)	(0.09%)	(0.07%)
Pure shear	Strength theory ($\bar{t}_{cr}^{\mathcal{F}}$)	150.61	23.08	106.80	98.53	23.08
	Phase-field fracture ($\bar{t}_{cr}^{PF}$)	147.49	22.97	105.99	98.10	22.97
		(−2.07%)	(−0.47%)	(−0.76%)	(−0.44%)	(−0.47%)

analytically derived as

$$\bar{t}_{cr}^{\mathcal{F}} = \begin{cases} \sigma_{ts} & \text{under uniaxial tension,} \\ \dfrac{2\sigma_{cs}\sigma_{ts}}{3\sigma_{cs} - \sigma_{ts}} & \text{under biaxial tension,} \\ \dfrac{2\sigma_{cs}\sigma_{ts}}{\sqrt{3}(\sigma_{cs} + \sigma_{ts})} & \text{under pure shear.} \end{cases}$$

In Table 2, we summarize the critical applied tractions ($\bar{t}_{cr}^{\mathcal{F}}$ and $\bar{t}_{cr}^{PF}$) for the five brittle materials from Table 1. The percentages in the parentheses are the relative errors of $\bar{t}_{cr}^{PF}$ with respect to $\bar{t}_{cr}^{\mathcal{F}}$. In all cases, the phase-field fracture theory agrees with the strength theory with a relative error of less than 3%. This is because the phase-field fracture theory predicts an identical strength surface as the strength theory when $\varepsilon \searrow 0$.

2.3.2. Mechanical domains with large pre-cracks

We now consider another type of representative mechanical domain — specimens with large pre-existing cracks. According to the strength criterion in (5), the critical applied traction (see Appendix A for derivation) is given as

$$\bar{t}_{cr}^{\mathcal{F}}(r) = \frac{1}{Y}\sqrt{\frac{2r}{a}} \sec\frac{\hat{\theta}}{2} \frac{2\sigma_{cs}\sigma_{ts}}{\sqrt{3}(\sigma_{cs} + \sigma_{ts})} \left[\sqrt{\frac{4}{3} - \cos^2\frac{\hat{\theta}}{2}} + \frac{2(\sigma_{cs} - \sigma_{ts})}{\sqrt{3}(\sigma_{cs} + \sigma_{ts})}\right]^{-1} \tag{8}$$

with

$$\hat{\theta} = 2\cos^{-1}\left[\frac{1}{2\sqrt{6}}\left(-3\gamma^2 + \gamma\sqrt{9\gamma^2 + 96} + 16\right)^{1/2}\right] \quad \text{and} \quad \gamma = \frac{2(\sigma_{cs} - \sigma_{ts})}{\sqrt{3}(\sigma_{cs} + \sigma_{ts})}.$$

In these expressions, the parameter a is the half crack length, and r is the distance between the material point of interest and the crack tip (Fig. 3(a)). The symbol Y is a dimensionless geometry-dependent parameter. Note that $\bar{t}_{cr}^{\mathcal{F}}$ is r-dependent, and it represents the minimum applied traction required to make a material point, located at a distance of r from the crack tip, violate the strength surface in (5).

Remark 5. Upon examining the strength-based critical applied traction in (8), one can observe that $\bar{t}_{cr}^{\mathcal{F}} \searrow 0$ as $r \searrow 0$. This limit analysis implies that fracture occurs immediately when an infinitesimal stress is applied to a cracked specimen, which is an *unrealistic* prediction. This prediction arises from the well-known stress singularity issue in (A.1) as $r \searrow 0$, indicating that elastostatics with a strength criterion is *insufficient* to predict fracture nucleation from large pre-existing cracks. This situation necessitates a new model for fracture prediction, such as LEFM.

Based on LEFM, fracture nucleation from large pre-existing cracks does not depend on the stress state of a single material point around the crack tip. Instead, it is controlled globally through the competition between strain and fracture energies. The critical applied traction is given by

$$\bar{t}_{cr}^{LEFM} = \frac{1}{Y}\sqrt{\frac{G_c E}{\pi a}}. \tag{9}$$

In the same vein, the phase-field fracture theory in (2)–(3) approximates the solution of (9) when fracture nucleates from large pre-existing cracks. We can derive its critical applied traction, $\bar{t}_{cr}^{PF}$, through a standard FEA.

We now compare the phase-field fracture theory and strength theory using numerical examples. As shown in Fig. 3(a), we consider a center-cracked rectangular specimen with geometries parameterized by the regularization length, ε. We uniformly apply traction loads, $\bar{t}$, to the top and bottom edges until the specimen fractures. To model the sharp crack, we simulate one-quarter of the domain using symmetry. To illustrate the differences between the phase-field fracture theory and strength theory, we use

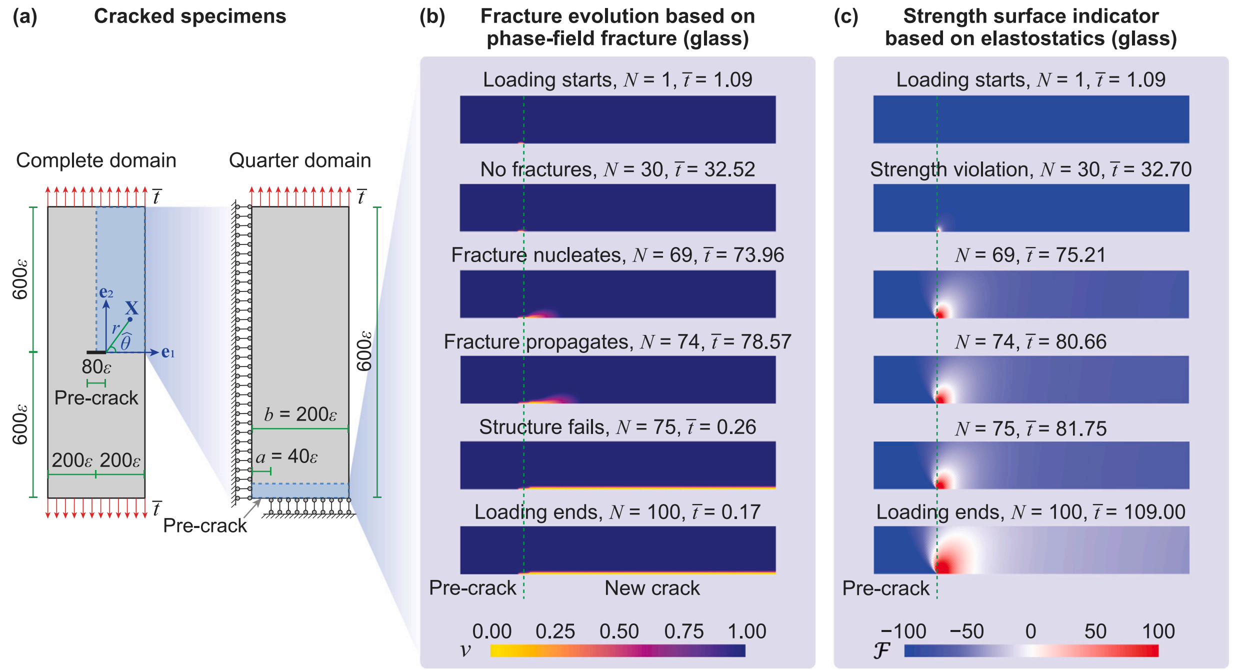

Fig. 3. Comparison between phase-field fracture and strength theories for mechanical domains with large pre-cracks. (a) Test specimens with large pre-cracks. The symbol $\mathbf{X}$ represents the material point of interest in the Cartesian ($\mathbf{e}_1$–$\mathbf{e}_2$) and polar (r–$\hat{\theta}$) coordinate systems. (b) Fracture evolution of the borosilicate glass material. The variables N and $\bar{t}$ are the load step counter and the amplitude of the applied traction (in MPa), respectively. The variable υ is the phase field with $\upsilon = 0$ representing the damage. (c) Strength surface indicator ($\mathcal{F}$) based on elastostatics. The value of $\mathcal{F}$ is limited to $[-100, 100]$ MPa for better visualization.

the borosilicate glass material in Table 1 as an example and implement the phase-field fracture model from (2)–(3) with standard FEA subject to 100 displacement-loading steps. At each load step, we back-calculate the equivalent applied traction, $\bar{t}$. During the simulation, we impose the "damaged notch condition" [56,79] by setting $\upsilon = 0$ in a small region ahead of the initial crack tip.

The fracture evolution at critical load steps is shown in Fig. 3(b). To compare it with the strength theory, we plot the strength surface indicator ($\mathcal{F}$) in Fig. 3(c) at the same load steps based on elastostatics. At step $N = 30$, the stress near the crack tip exceeds the strength surface; however, no fracture occurs at this stage. Fracture nucleation initiates at step $N = 69$ and propagates by step $N = 74$, leading to instantaneous structural failure at load step $N = 75$ due to the rapid development of a transverse crack. This failure state persists until the final load step, $N = 100$, which lies beyond the predictive scope of strength theory.

Next, we quantitatively compare the critical applied tractions of LEFM ($\bar{t}^{\mathrm{LEFM}}_{\mathrm{cr}}$), phase-field fracture theory ($\bar{t}^{\mathrm{PF}}_{\mathrm{cr}}$), and strength theory ($\bar{t}^{\mathcal{F}}_{\mathrm{cr}}$) for all materials in Table 1. For the specimen geometry and boundary conditions in Fig. 3(a), the geometry factor Y in (8) and (9) is given as [80]

$$Y(a/b) = \left[1 - 0.025\left(\frac{a}{b}\right)^2 + 0.06\left(\frac{a}{b}\right)^4\right]\sqrt{\sec\left(\frac{\pi a}{2b}\right)}$$

where b is the half domain width. To compute $\bar{t}^{\mathrm{PF}}_{\mathrm{cr}}$, we associate it with the instance when the phase field at the material point $(\varepsilon, 0)$ satisfies $\upsilon = 0$, indicating fracture nucleation around the crack tip (Fig. 3(b)). As for the computation of $\bar{t}^{\mathcal{F}}_{\mathrm{cr}}$, it has been discussed that $\bar{t}^{\mathcal{F}}_{\mathrm{cr}} \searrow 0$ as $r \searrow 0$. However, for the stress-constrained topology optimization that will be introduced later, it is also meaningful to examine the value of $\bar{t}^{\mathcal{F}}_{\mathrm{cr}}$ at some finite distance r. Here, we choose $r = \varepsilon$.

In Table 3, we summarize the critical applied tractions ($\bar{t}^{\mathrm{LEFM}}_{\mathrm{cr}}$, $\bar{t}^{\mathrm{PF}}_{\mathrm{cr}}$, and $\bar{t}^{\mathcal{F}}_{\mathrm{cr}}$) for the five brittle materials listed in Table 1. The percentages in parentheses represent the relative errors compared to the LEFM solution ($\bar{t}^{\mathrm{LEFM}}_{\mathrm{cr}}$). Notably, the critical applied traction predicted by the phase-field fracture theory ($\bar{t}^{\mathrm{PF}}_{\mathrm{cr}}$) closely aligns with the LEFM solution ($\bar{t}^{\mathrm{LEFM}}_{\mathrm{cr}}$) with relative errors less than 6%. Conversely, the critical applied traction predicted by the strength theory deviates from the LEFM solution ($\bar{t}^{\mathrm{LEFM}}_{\mathrm{cr}}$), underestimating the fracture resistance of structures even at a finite distance ($r = \varepsilon$) from the crack tip.

2.3.3. Summary of the comparisons

After comparing the phase-field fracture and strength theories, we summarize their fracture predictions as follows. Specifically, the phase-field fracture theory in (2)–(3) considers fracture nucleation

- in the body of the design domain under a *uniform* stress state is controlled by a built-in strength surface of materials ($\mathcal{F}^{\varepsilon} = 0$ in (7)),

Table 3
Critical applied tractions of the center-cracked specimen (unit: MPa).

Failure criteria	Borosilicate glass	Graphite	Titania	PMMA	Artificial
LEFM ($\bar{t}_{\rm cr}^{\rm LEFM}$)	73.89	18.39	72.77	95.86	18.39
Phase-field fracture ($\bar{t}_{\rm cr}^{\rm PF}$)	73.96 (0.09%)	18.27 (−0.63%)	68.40 (−6.00%)	90.44 (−5.66%)	18.27 (−0.63%)
Strength theory ($\bar{t}_{\rm cr}^{\mathcal{F}}$)	22.90 (−69.01%)	4.37 (−76.23%)	14.94 (−79.47%)	21.56 (−77.51%)	4.37 (−76.23%)

- from large pre-existing cracks is governed by Griffith's competition [58] between strain energy (through $W(\mathbf{E})$) and fracture energy (through G_c),
- in all other scenarios involves the interaction [56] between the material's strength surface and Griffith's energy competition.

Additionally, the phase-field fracture theory considers that fracture propagation

- is also governed by Griffith's energy competition.

As for the strength theory in (5), it identifies the fracture nucleation whenever

- the strength surface of materials is violated ($\mathcal{F} > 0$) irrespective of the uniformity of the stress state or the geometric singularities.

Moreover, the strength theory does *not* account for fracture propagation. In the next sections, we will recap and examine topology optimization formulations based on the phase-field fracture and strength theories, where the differences between the two fracture criteria become more pronounced.

3. Stress-constrained and fracture-based topology optimization

In this section, we present the stress-constrained [21] and fracture-based [7] topology optimization formulations, with the corresponding algorithms provided in Appendix B. These formulations are built upon the state equations established in Section 2 and will be compared in Section 4.

3.1. Design space parameterization

To proceed with both stress-constrained and fracture-based topology optimization, we begin by parameterizing the design space [3]. Specifically, we define a dimensionless and continuous scalar field, $\rho(\mathbf{X}) \in [0,1]$, as the design variable. To alleviate the mesh dependency and avoid the checkerboard patterns of the optimized designs, we apply a linear filter [81] and derive the filtered design variable as

$$\widetilde{\rho}(\mathbf{X}) = \frac{\displaystyle\int_\Omega w(\mathbf{X},\mathbf{X}')\rho(\mathbf{X}')\mathrm{d}\mathbf{X}'}{\displaystyle\int_\Omega w(\mathbf{X},\mathbf{X}')\mathrm{d}\mathbf{X}'} \tag{10}$$

where the coefficient $w(\mathbf{X},\mathbf{X}') = \max\{0, R - |\mathbf{X}-\mathbf{X}'|\}$ is a weighting factor determined by the filter radius ($R > 0$) and the Euclidean distance ($|\mathbf{X}-\mathbf{X}'|$) between material points $\mathbf{X}$ and $\mathbf{X}'$. To promote solid–void optimized designs, we further apply a Heaviside projection [82] on the filtered design variable ($\widetilde{\rho}$) and derive the projected (or physical) design variable as

$$\overline{\rho}(\mathbf{X}) = \frac{\tanh(\beta\theta) + \tanh(\beta(\widetilde{\rho}(\mathbf{X}) - \theta))}{\tanh(\beta\theta) + \tanh(\beta(1-\theta))} \tag{11}$$

where β is the sharpness parameter, and $\theta = 0.5$ is the projection threshold. The projected design variable describes the material distribution with $\overline{\rho}(\mathbf{X}) = 0$ being void and $\overline{\rho}(\mathbf{X}) = 1$ being solid.

3.2. Stress-constrained topology optimization

3.2.1. Material property interpolation

After design space parameterization, we introduce the material property interpolation for the stress-constrained topology optimization formulation. Precisely, we specify

$$E(\overline{\rho}) = [\eta_E + (1-\eta_E)\overline{\rho}^{p_E}]E_0 \quad \text{and} \quad \nu(\overline{\rho}) \equiv \nu_0 \tag{12}$$

based on the modified version [4] of the method of solid isotropic material with penalization (SIMP) [3]. In these expressions, the constants E_0 and ν_0 represent the Young's modulus and Poisson's ratio of the solid material ($\overline{\rho} = 1$), respectively. The parameter $\eta_E = 10^{-6}$ is a sufficiently small positive number to prevent the singularity of the stiffness matrix. The parameter $p_E = 3$ penalizes intermediate projected design variable ($\bar{\rho} \in (0,1)$). The variables $E(\bar{\rho})$ and $\nu(\bar{\rho})$ are the interpolated Young's modulus and Poisson's ratio, respectively, and they can be converted to the interpolated Lamé constants ($\lambda(\bar{\rho})$ and $\mu(\bar{\rho})$) through

$$\lambda(\bar{\rho}) = \frac{E(\bar{\rho})\nu(\bar{\rho})}{(1+\nu(\bar{\rho}))(1-2\nu(\bar{\rho}))} \quad \text{and} \quad \mu(\bar{\rho}) = \frac{E(\bar{\rho})}{2(1+\nu(\bar{\rho}))}.$$

Additionally, we can interpolate the material strength surface in (5) as

$$\widehat{\mathcal{F}}(I_{1,0}, J_{2,0}) = [\eta_E + (1-\eta_E)\bar{\rho}^{p_E}]\Lambda(I_{1,0}, J_{2,0}) = 0$$

with

$$\Lambda(I_{1,0}, J_{2,0}) := \frac{\sqrt{3}(\sigma_{\mathrm{cs},0} + \sigma_{\mathrm{ts},0})}{2\sigma_{\mathrm{cs},0}\sigma_{\mathrm{ts},0}}\sqrt{J_{2,0}} + \frac{\sigma_{\mathrm{cs},0} - \sigma_{\mathrm{ts},0}}{2\sigma_{\mathrm{cs},0}\sigma_{\mathrm{ts},0}} I_{1,0} - 1$$

where

$$I_{1,0} := \frac{E_0}{1-2\nu_0}\mathrm{tr}[\mathbf{E}(\mathbf{u})] \quad \text{and} \quad J_{2,0} := \frac{E_0^2}{4(1+\nu_0)^2}\mathrm{tr}[\mathbf{E}_D^2(\mathbf{u})].$$

In these expressions, the constants $\sigma_{\mathrm{ts},0}$ and $\sigma_{\mathrm{cs},0}$ are the uniaxial tensile and compressive strengths of the solid material ($\bar{\rho} = 1$), respectively.

3.2.2. Topology optimization formulation

Based on the above setup, we present the stress-constrained topology optimization formulation as

$$\begin{cases} \underset{0\le\rho\le1}{\text{maximize}} & \Pi(\bar{\rho}, \mathbf{u}(\bar{\rho})) = \displaystyle\int_\Omega W(\mathbf{E}(\mathbf{u}); \bar{\rho})\mathrm{d}\mathbf{X}; \\ \text{subject to} & \begin{cases} g_{1,e}(\bar{\rho}, \mathbf{u}(\bar{\rho})) = [\eta_E + (1-\eta_E)\bar{\rho}_e^{p_E}]\Lambda_e(\Lambda_e^2 + 1) \le 0 \quad \text{for} \quad e = 1, \ldots, N^{\mathtt{elem}}; \\ g_2(\bar{\rho}) = \dfrac{1}{|\Omega|}\displaystyle\int_\Omega \bar{\rho}\mathrm{d}\mathbf{X} - V^* \le 0; \\ \text{equilibrium equations in (1).} \end{cases} \end{cases} \tag{13}$$

In this formulation, we maximize the structural stiffness by maximizing the total strain energy (Π) under the displacement loading (see discussion about "maximizing" energy in Appendix C). Additionally, we impose the polynomial-vanishing [20] stress constraints ($g_{1,e} \le 0$) at each element centroid ($N^{\mathtt{elem}}$ elements in total) with an AL-based formulation that preserves the local nature of the stress [21,28,66]. Finally, we impose a material volume constraint ($g_2 \le 0$) with V^* representing the allowable material volume fraction. The detailed algorithm of the stress-constrained formulation in (13) is provided in Appendix B.1.

The selection of the stress-constrained topology optimization in (13) merits further explanation. Classical stress-based formulations typically minimize material usage while satisfying a stress constraint [20,21,23,83], which generally ensures a converged optimized design by implicitly setting the allowable volume fraction to its maximum, $V^* = 1$. In contrast, the stress-based formulation in (13) aims to maximize structural stiffness while constraining both stress states and material usage. This choice is motivated by three key reasons. First, explicitly maximizing strain energy/stiffness (alternatively setting additional constraints to ensure minimal stiffness) is necessary to form a structure when the design domain is subjected to displacement-controlled (rather than force-controlled) loadings. Second, the formulation in (13) aligns with scenarios involving limited material availability, as in other topology optimization problems [4,8,84]. Finally, it allows for a more direct comparison with the fracture-based formulation in (16) that will be introduced later, where both formulations share the objective of maximizing structural initial stiffness. Different from minimizing the material volume (with additional minimal stiffness constraints), maximizing strain energy/stiffness encourages the optimized designs from both formulations to utilize all available materials, which enables a consistent comparison of structural performances (i.e., initial stiffness, effective toughness, and the crack displacement) of different optimized designs. However, we emphasize that, when using either the stress-constrained or fracture-based formulation independently, users retain the flexibility to modify the objective and constraint functions for specific design requirements.

3.3. Fracture-based topology optimization

In this section, we introduce another type of topology optimization formulation [7] for controlling fracture behaviors, which is built upon the phase-field fracture theory [56] summarized in Section 2.2.

3.3.1. Material property interpolation

We begin by interpolating the fracture-related material properties (E, ν, G_c, σ_{cs}, and σ_{ts}) as

$$\begin{cases} E(\bar{\rho}) = \dfrac{1}{\sqrt{s(\bar{\rho})}}[\eta_E + (1-\eta_E)\bar{\rho}^{p_E}]E_0, \quad \nu(\bar{\rho}) \equiv \nu_0, \quad G_c(\bar{\rho}) = \dfrac{1}{\sqrt{s(\bar{\rho})}}[\eta_{G_c} + (1-\eta_{G_c})\bar{\rho}^{p_{G_c}}]G_{c,0}, \\ \sigma_{\mathrm{cs}}(\bar{\rho}) = [\eta_{\mathrm{cs}} + (1-\eta_{\mathrm{cs}})\bar{\rho}^{p_\sigma}]\sigma_{\mathrm{cs},0}, \quad \sigma_{\mathrm{ts}}(\bar{\rho}) = [\eta_{\mathrm{ts}} + (1-\eta_{\mathrm{ts}})\bar{\rho}^{p_\sigma}]\sigma_{\mathrm{ts},0} \end{cases} \tag{14}$$

with a scaling factor [7]

$$s(\overline{\rho}) = \frac{[\eta_E + (1-\eta_E)\overline{\rho}^{p_E}][\eta_{G_c} + (1-\eta_{G_c})\overline{\rho}^{p_{G_c}}]}{[\eta_{\text{ts}} + (1-\eta_{\text{ts}})\overline{\rho}^{p_\sigma}]^2}. \tag{15}$$

The variables E_0, ν_0, $G_{c,0}$, $\sigma_{\text{cs},0}$, and $\sigma_{\text{ts},0}$ are properties of the solid material ($\overline{\rho} = 1$). The parameters η_E, η_{Gc}, η_{cs}, and η_{ts} take sufficiently small positive values to prevent the singularity when $\overline{\rho} = 0$. The parameters p_E, p_{G_c}, and p_σ penalize the elasticity (E), critical energy release rate (G_c), and strengths (σ_{cs} and σ_{ts}) when $\overline{\rho} \in (0,1)$, respectively.

Remark 6. The phase-field fracture model in (2)–(3) implicitly features a material length scale

$$\varepsilon_c = \frac{3G_c E}{8\sigma_{\text{ts}}^2}$$

when the uniaxial tensile strength (σ_{ts}) is dominant. This material length scale can be made independent of $\overline{\rho}$ with the material property interpolation rules in (14) with (15) because

$$\varepsilon_c(\overline{\rho}) = \frac{3G_c(\overline{\rho})E(\overline{\rho})}{8\sigma_{\text{ts}}^2(\overline{\rho})} = \frac{3}{8}\frac{\left\{\frac{1}{\sqrt{s(\overline{\rho})}}[\eta_{G_c} + (1-\eta_{G_c})\overline{\rho}^{p_{G_c}}]G_{c,0}\right\}\left\{\frac{1}{\sqrt{s(\overline{\rho})}}[\eta_E + (1-\eta_E)\overline{\rho}^{p_E}]E_0\right\}}{\left\{[\eta_{\text{ts}} + (1-\eta_{\text{ts}})\overline{\rho}^{p_\sigma}]\sigma_{\text{ts},0}\right\}^2} \equiv \frac{3G_{c,0}E_0}{8\sigma_{\text{ts},0}^2}.$$

Remark 7. To make $E(\overline{\rho})$ in (14) close to the modified version [4] of the SIMP rule [3] for elasticity, which has shown effective penalization of intermediate values of $\overline{\rho}$ and (approximated) satisfaction of physical bounds of elasticity for various $\overline{\rho}$ values, we enforce

$$s(0) = 1 \quad \Rightarrow \quad \eta_E \eta_{G_c} = \eta_{\text{ts}}^2$$

for $\overline{\rho} = 0$ and

$$s(\overline{\rho}) = \frac{\overline{\rho}^{p_E}\overline{\rho}^{p_{G_c}}}{\overline{\rho}^{2p_\sigma}} = 1 \quad \Rightarrow \quad p_E + p_{G_c} = 2p_\sigma$$

for $\overline{\rho} \in (0,1]$ as $\eta_E \searrow 0$, $\eta_{G_c} \searrow 0$, and $\eta_{\text{ts}} \searrow 0$.

Remark 8. A fracture may occur due to the relatively small strength in the regions of $\overline{\rho} \searrow 0$. To avoid such artificial behavior, we require

$$p^\sigma < p^E,$$

which is akin to the relaxation scheme in [19]. Additionally, to eliminate the artificial higher compressive strength when $\overline{\rho} \searrow 0$, we enforce

$$\sigma_{\text{cs}}(0) = \sigma_{\text{ts}}(0) \quad \Rightarrow \quad \eta_{\text{cs}}\sigma_{\text{cs},0} = \eta_{\text{ts}}\sigma_{\text{ts},0}.$$

3.3.2. Topology optimization formulation

After material property interpolation, we present the fracture-based topology optimization formulation as [7]

$$\begin{cases} \underset{0\le\rho\le1}{\text{maximize}} & J(\overline{\rho}; \mathbf{u}_1, \mathbf{u}_2, \dots, \mathbf{u}_N; v_1, v_2, \dots, v_N) = \omega_e \Pi_e - \omega_f \Pi_f + \omega_w \Pi_w; \\ \text{subject to} & \begin{cases} g(\overline{\rho}) = \frac{1}{|\Omega|}\int_\Omega \overline{\rho}\,\mathrm{d}\mathbf{X} - V^* \le 0; \\ \text{equilibrium equations in (2)–(3).} \end{cases} \end{cases} \tag{16}$$

In this formulation, we maximize the weighted sum of the integrated elastic energy (Π_e), integrated fracture energy (Π_f), and total work (Π_w) through the weights, ω_e, ω_f, and ω_w, respectively. These three energy terms are defined as

$$\begin{cases} \Pi_e = \frac{1}{2}\sum_{k=1}^{n}(t_k - t_{k-1})\int_\Omega \left[v_{k-1}^2 W(\mathbf{E}(\mathbf{u}_{k-1}); \overline{\rho}) + v_k^2 W(\mathbf{E}(\mathbf{u}_k); \overline{\rho})\right]\mathrm{d}\mathbf{X} \\ \Pi_f = \frac{1}{2}\sum_{k=1}^{n}(t_k - t_{k-1})\int_\Omega \frac{3G_c(\overline{\rho})}{8}\left[\left(\frac{1-v_{k-1}}{\varepsilon} + \varepsilon\nabla v_{k-1}\cdot\nabla v_{k-1}\right) + \left(\frac{1-v_k}{\varepsilon} + \varepsilon\nabla v_k\cdot\nabla v_k\right)\right]\mathrm{d}\mathbf{X} \\ \Pi_w = \frac{1}{2}\sum_{k=n+1}^{N}\int_{\partial\Omega}\left[v_{k-1}^2\frac{\partial W}{\partial\mathbf{E}}(\mathbf{E}(\mathbf{u}_{k-1}); \overline{\rho}) + v_k^2\frac{\partial W}{\partial\mathbf{E}}(\mathbf{E}(\mathbf{u}_k); \overline{\rho})\right]\mathbf{N}\cdot(\mathbf{u}_k - \mathbf{u}_{k-1})\mathrm{d}\mathbf{X} \end{cases} \tag{17}$$

where n is a critical load step of selection, and N is the number of all load steps. In the fracture-based formulation in (16), we adopt the same material volume constraint (g) as the stress-constrained one in (13). In accordance with [7], we will consistently use (16)

Table 4
Model inputs (extracted from [7]) for the stress-constrained and fracture-based formulations.

Model inputs	Stress-constrained formulation	Fracture-based formulation
Young's modulus (E)	$E_0 = 980$ MPa	$E_0 = 980$ MPa
	$\eta_E = 10^{-6}$	$\eta_E = 10^{-5}$
	$p_E = 3$	$p_E = 3$
Poisson's ratio (ν)	$\nu_0 = 0.13$	$\nu_0 = 0.13$
Compressive strength (σ_{cs})	$\sigma_{\mathrm{cs},0} = 77$ MPa	$\sigma_{\mathrm{cs},0} = 77$ MPa
	–	$\eta_{\mathrm{cs}} = 3.51 \times 10^{-6}$
	–	$p_\sigma = 2.5$
Tensile strength (σ_{ts})	$\sigma_{\mathrm{ts},0} = 27$ MPa	$\sigma_{\mathrm{ts},0} = 27$ MPa
	–	$\eta_{\mathrm{ts}} = 10^{-5}$
	–	$p_\sigma = 2.5$
Critical energy release rate (G_c)	–	$G_{c,0} = 0.91$ N/mm
	–	$\eta_{G_c} = 10^{-5}$
	–	$p_{G_c} = 2$
Regularization length (ε)	–	$\varepsilon = 0.15$ mm
Calibrated parameter (δ^ε)	–	$\delta^\varepsilon = 6.48$

for all fracture-based designs in Section 4 except for the `fracture 2` design in Fig. 6(b), where we reformulate (16) as

$$\begin{cases} \underset{0\le\rho\le 1}{\text{maximize}} & J(\overline{\rho};\mathbf{u}_1,\mathbf{u}_2,\ldots,\mathbf{u}_N;v_1,v_2,\ldots,v_N) = \Pi_e; \\ \text{subject to} & \begin{cases} g_1(\overline{\rho};v_1,v_2,\ldots,v_N) = \Pi_f = 0; \\ g_2(\overline{\rho}) = \dfrac{1}{|\Omega|}\displaystyle\int_\Omega \overline{\rho}\,\mathrm{d}\mathbf{X} - V^* \le 0; \\ \text{equilibrium equations in (2)–(3).} \end{cases} \end{cases} \tag{18}$$

to make it analogous to the stress-constrained formulation in (13). The detailed algorithm of the fracture-based formulations in (16) and (18) are provided in Appendix B.2.

Remark 9. The phase-field fracture theory in (2)–(3) utilizes a *scaled* strain energy density, $v_k^2 W(\mathbf{E}(\mathbf{u}_k))$, to capture the damage in elasticity due to fracture. This scaled strain energy density exhibits nonlinearity with respect to the loading time, t_k. To address this nonlinearity, the fracture-based formulation in (16) optimizes the area under the scaled strain energy–time curve. In contrast, the strain energy density in elastostatics (Eq. (1)) is linear with respect to loading time. As a result, the stress-constrained formulation (Eq. (13)) can directly optimize the *non-scaled*, *end* strain energy density, $W(\mathbf{E}(\mathbf{u}))$.

4. Sample examples for comparing the two formulations

In this section, we systematically compare the stress-constrained and fracture-based topology optimization formulations by examining their optimized designs for three groups of benchmark examples. Specifically, Section 4.1 compares the optimized designs for intact and notched beams under three-point bending. The intact beam features fracture nucleation from smooth boundaries, whereas the notched beam highlights fracture nucleation from large pre-existing cracks. Next, Section 4.2 examines T-shaped corbels with equal and unequal tension–compression strengths of the material. These corbels demonstrate the fracture nucleation from sharp corners, and here we also examine the residual fracture resistance of optimized designs after the first crack occurrence. Finally, Section 4.3 evaluates the designs' performance for an unnotched column under uniaxial tension and a notched column under Mode I loading. The former features fracture nucleation from the bulk of materials, and the latter once again features fracture nucleation from large pre-existing cracks. For all examples, we consistently employ the model inputs in Table 4 (extracted from [7]) unless stated otherwise.

To quantify the structural responses of the optimized designs, we consistently use the following metrics. To determine the initial stiffness (K), we define

$$K = \frac{2}{\overline{u}_1^2}\int_\Omega W(\mathbf{E}(\mathbf{u}_1))\mathrm{d}\mathbf{X},$$

where $\mathbf{u}_1(\mathbf{X}) = \mathbf{u}(\mathbf{X}, t_1)$ and $\overline{u}_1 = \overline{u}(t_1)$ are the displacement field ($\mathbf{u}$) and the amplitude of the applied displacement ($\overline{u}$) at the first load step, respectively. To capture the critical applied displacement (u_c) when the first fracture occurs, we define

$$u_c = \min\{\overline{u}(t_{k-1}) | F(\overline{u}(t_{k-1})) > F(\overline{u}(t_k))\},$$

where F represents the resultant reaction force. Note that u_c corresponds to the first drop of the F–$\overline{u}$ curve. To compute the effective toughness (Ψ) of the structures, we define

$$\Psi = \frac{1}{2}\sum_{k=1}^{N}\frac{F(\overline{u}(t_k)) + F(\overline{u}(t_{k-1}))}{\overline{u}(t_k) - \overline{u}(t_{k-1})},$$

Table 5
Topology optimization parameters of stress-constrained and fracture-based formulations.

Examples	Designs	Volume fractions (V^*)	Filter radii (R in mm)	Weighting factors ($\omega_e : \omega_f : \omega_w$)	Target fracture displacements (u_a or u_n in mm)
Section 4.1.1: Intact beam	Stiffness	0.45	1.20	–	–
	Stress	0.45	1.20	–	2.40
	Fracture 1	0.45	1.20	0.20 : 0.80 : 0.00	2.40
	Fracture 2	0.45	1.20	0.20 : 0.80 : 0.00	2.80
Section 4.1.2: Notched beam	Stiffness	0.45	1.50	–	–
	Stress	0.45	1.50	–	1.60
	Fracture 1	0.45	1.50	0.20 : 0.80 : 0.00	1.60
	Fracture 2	0.45	1.50	–	1.60
Section 4.2.1: Corbel with equal strengths	Stiffness	0.40	0.25	–	–
	Stress	0.40	0.25	–	0.60
	Fracture	0.40	0.25	0.20 : 0.80 : 0.00	0.60
Section 4.2.2: Corbel with unequal strengths	Stiffness	0.40	0.25	–	–
	Stress	0.40	0.25	–	0.70
	Fracture 1	0.40	0.25	0.15 : 0.85 : 0.00	0.70
	Fracture 2	0.40	0.25	0.10 : 0.90 : 0.00	0.90
	Fracture 3	0.40	0.25	0.25 : 0.55 : 0.20	0.60
Section 4.3.1: Unnotched column	Stiffness	0.40	0.30	–	–
	Stress	0.40	0.30	–	0.25
	Fracture 1	0.40	0.30	0.20 : 0.80 : 0.00	0.25
	Fracture 2	0.40	0.30	0.20 : 0.70 : 0.10	0.40
Section 4.3.2: Notched column	Stiffness	0.80	0.60	–	–
	Stress	0.80	0.60	–	0.15
	Fracture	0.80	0.60	0.05 : 0.70 : 0.25	0.05

which denotes the area below the F–$\bar{u}$ curve of optimized designs. Similarly, we define the post-fracture effective toughness (Ψ_l) as

$$\Psi_l = \frac{1}{2}\sum_{k=l+1}^{N} \frac{F(\bar{u}(t_k)) + F(\bar{u}(t_{k-1}))}{\bar{u}(t_k) - \bar{u}(t_{k-1})},$$

where l is the load step corresponding to the first fracture occurrence (u_c). In all subsequent numerical examples, we define $\bar{u}$ as the amplitude of the final applied displacement. In the fracture-based formulation, we set $u_n \in [0, \bar{u}]$ as the lower bound of the fracture displacement, corresponding to the critical load step (n) in (17). In the stress-constrained formulation, we define the counterpart as $u_a = \bar{u}$, and the stress remains within the strength surface ($\mathcal{F} = 0$) up to this displacement.

Based on the model inputs in Table 4 and the performance measurements (K, u_c, Ψ, and Ψ_l) defined above, we proceed with the comparative study. To solve the elastostatics problem in (1), we use a direct solver to derive the displacement field. For the phase-field fracture problem in (2)–(3), we decouple it into two subproblems with a staggered strategy (alternating minimization). We solve the displacement subproblem in (2) with a direct solver, and the phase-field subproblem in (3) using the Newton–Raphson scheme and the generalized minimal residual (GMRES) algorithm [85].

To perform the stress-constrained and fracture-based topology optimization, we utilize the adjoint method [4] to evaluate the sensitivities and employ the method of moving asymptotes (MMA) [86] to update the design variable ($\rho(\mathbf{X})$). The key topology optimization parameters of the two formulations are summarized in Table 5. The stress-constrained formulation is implemented in MATLAB, while the fracture-based formulation is implemented by generalizing FEniTop[2] [87] (FEniCSx-based [88] topology optimization). Following topology optimization, we perform the fracture analysis for all designs with (2)–(3) based on the body-fitted mesh with the same element size as the fixed-grid mesh used in topology optimization. The optimized designs of both formulations are presented below, and a summary of computational costs is provided in Appendix D.

4.1. Intact and notched beams under three-point bending

In this section, we compare the two formulations by analyzing their optimized designs for intact and notched beams under three-point bending. These two design domains — featuring fracture nucleation from smooth boundaries and large pre-existing cracks, respectively — serve as fundamental tests for assessing the effectiveness of the two formulations in enhancing brittle fracture resistance.

[2] The open-source code is available at https://github.com/missionlab/fenitop.

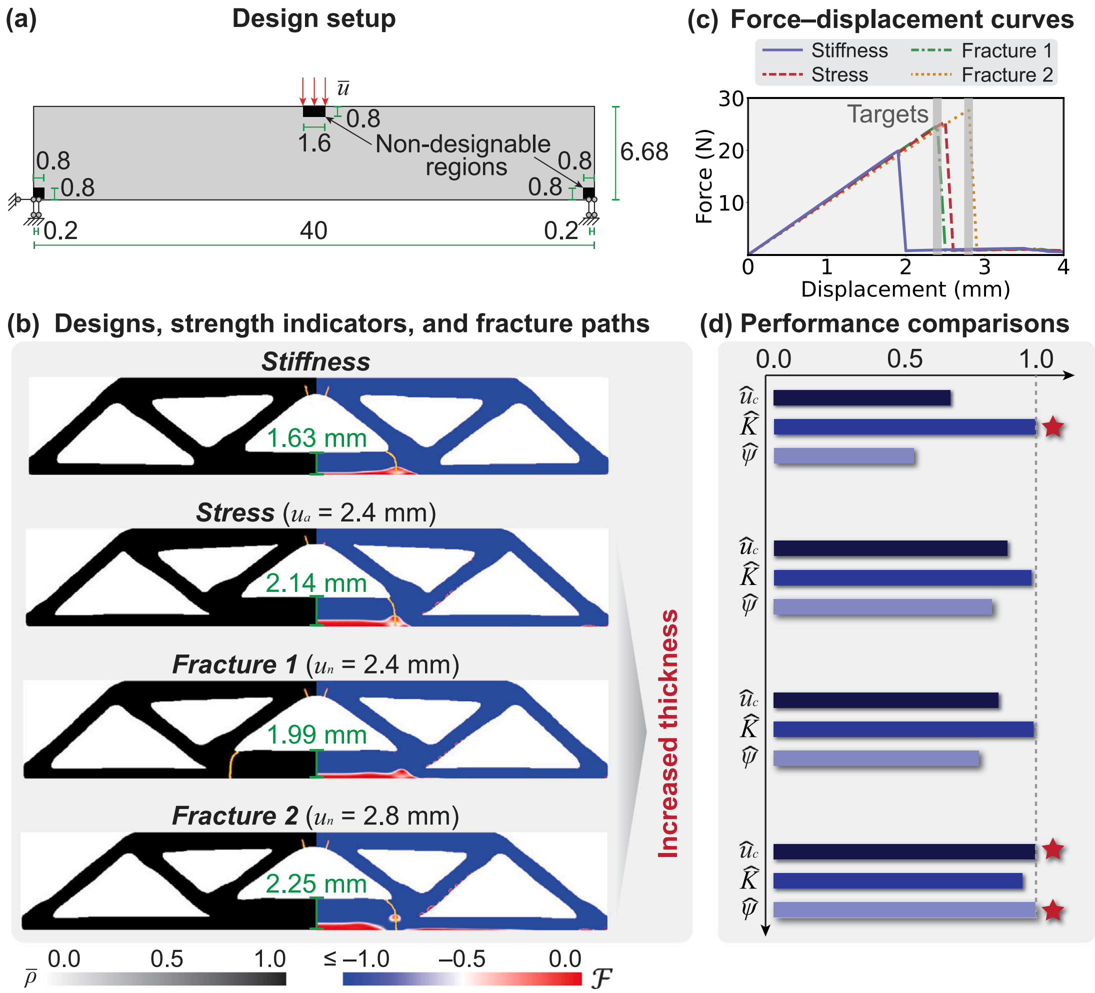

Fig. 4. Comparison among the optimized stiffness, stress, and fracture designs for an intact beam under three-point bending. (a) Design setup including the design domain and boundary conditions. The geometries are in a unit of mm. The variable $\bar{u}$ is the amplitude of the applied displacement ($\bar{\mathbf{u}}$). (b) Optimized designs ($\bar{\rho}$), strength surface indicators ($\mathcal{F}$), and fracture paths. The strength surface indicators are plotted for $\mathcal{F} \in [-1, 0]$ MPa at the load step immediately preceding the first fracture propagation, while the fracture paths are depicted at the final load step and determined using the phase-field fracture theory in (2)–(3). The green text represents the member thickness. (c) Force–displacement (F–$\bar{u}$) responses of the optimized designs. (d) Comparisons of the normalized performance measurements, $\hat{u}_c = u_c/\max(u_c)$, $\hat{K} = K/\max(K)$, and $\hat{\Psi} = \Psi/\max(\Psi)$. (For interpretation of the references to color in this figure legend, the reader is referred to the web version of this article.)

4.1.1. Intact beam under three-point bending

We begin by considering the intact beam under three-point bending as shown in Fig. 4(a). To perform topology optimization, we discretize the design domain with a structured mesh consisting of 120,000 first-order quadrilateral elements of size $h = 0.05$ mm. For both formulations, we adopt a volume fraction of $V^* = 0.45$ and a filter radius of $R = 1.2$ mm. After topology optimization, we perform the fracture analysis in (2)–(3) for all optimized designs based on body-fitted meshes.

The optimized designs, strength surface indicators, and fracture paths are shown in Fig. 4(b). For reference, we present one stiffness-maximization design (labeled as `stiffness`), which is obtained by deactivating the stress constraint in (13). Additionally, we display one stress-constrained design (labeled as `stress`) with a target fracture displacement of $u_a = 2.4$ mm. We also present two fracture-based designs with critical displacements of $u_n = 2.4$ mm (labeled as `fracture 1`) and $u_n = 2.8$ mm (labeled as `fracture 2`), respectively. Based on Fig. 4(b), all optimized designs share the same topology. However, compared to the `stiffness` design, which has a bottom member thickness of 1.63 mm, the `stress` design requires a thicker member at 2.14 mm. The two fracture designs also exhibit larger thicknesses, with `fracture 1` at 1.99 mm and `fracture 2` at 2.25 mm. This increase in member thickness reduces the average tensile stress along the longitudinal direction, thereby delaying fracture nucleation. To quantitatively compare the performance of the optimized designs, we present the force–displacement (F–$\bar{u}$) curves in Fig. 4(c) and display the normalized performance measurements ($\hat{u}_c = u_c/\max(u_c)$, $\hat{K} = K/\max(K)$, and $\hat{\Psi} = \Psi/\max(\Psi)$) in Fig. 4(d). Several observations can be made as follows. First, compared to the `stiffness` design ($u_c = 1.9$ mm), both the `stress` and `fracture 1` designs effectively delay fracture nucleation to $u_c = 2.5$ mm and $u_c = 2.4$ mm, respectively, meeting the target value of 2.4 mm. Second,

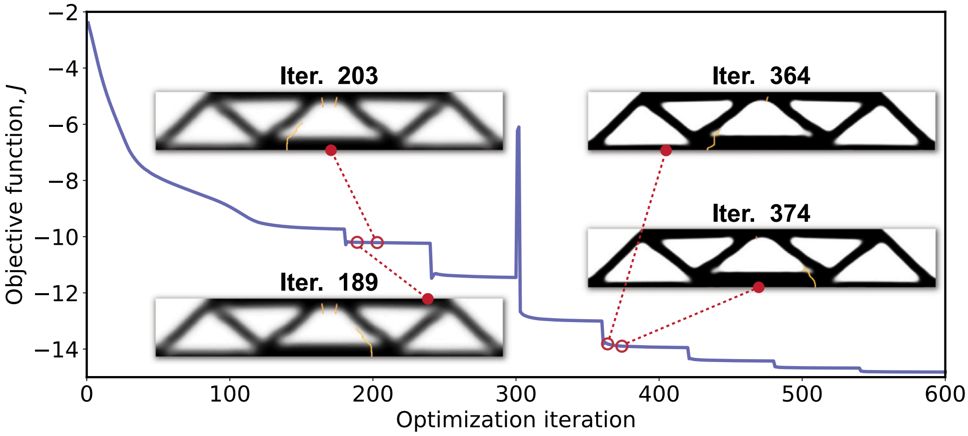

Fig. 5. The history of the objective function (J) for `fracture 1` in Fig. 4(b).

with a critical displacement of $u_n = 2.8$ mm, the `fracture 2` design further delays fracture nucleation to $u_c = 2.8$ mm. The stress-constrained formulation fails to generate a converged design for $u_a = 2.8$ mm, which is due to the volume constraint imposed on the optimization problem in (13) as discussed in Section 3.2.2. Finally, all optimized designs exhibit similar initial stiffness (K), while the `fracture 2` design demonstrates the largest effective toughness (Ψ) due to the delayed onset of fracture.

We reiterate that the design domains and optimized structures in this example feature fracture nucleation from smooth boundaries, which is governed by both the material's strength surface ($\mathcal{F} = 0$) and critical energy release rate (G_c) [56]. For moderately large target fracture displacements (2.4 mm in this case), both the stress-constrained and fracture-based formulations are effective, producing optimized designs with comparable fracture performance. However, under a larger target fracture displacement (2.8 mm in this case), the fracture-based formulation continues to generate converged designs with the desired fracture behavior, demonstrating greater flexibility. In contrast, the stress-constrained formulation shows the difficulty in preventing the strength surface violation and struggles to produce converged designs. In this case, the enforcement of stress constraints becomes an overly strict condition for ensuring fracture resistance, as the violation of the strength surface ($\mathcal{F} > 0$) under a *non-uniform* stress state does not necessarily trigger fracture nucleation [74].

Remark 10. The optimized designs in Fig. 4(b) exhibit different fracture locations in the bottom members due to several factors. Mathematically, the phase-field fracture problem in (16) is inherently non-convex [56,75] and allows for multiple solution pairs of $(\mathbf{u}_k(\mathbf{X}), v_k(\mathbf{X}))$. Computationally, while plane symmetry is enforced in the optimized design ($\overline{\rho}(\mathbf{X})$) and boundary conditions, the displacement and phase fields prior to fracture onset may exhibit slight asymmetry due to rounding errors in floating-point operations on modern computers. Consequently, fracture nucleation can occur on either the left or right side, echoing the stochastic nature of fracture observed in real-world structures. Importantly, this variation in nucleation position generally does not impact key fracture performance metrics ($\widehat{u}_c$, $\widehat{K}$, and $\widehat{\Psi}$), as shown by the smooth convergence history of the objective function in Fig. 5. Moreover, for explicit control over this randomness, one can introduce a stochastic distribution of material strengths (e.g., Fig. 11(b) in [89]) to capture nondeterministic fracture paths in practical applications.

4.1.2. Notched beam under three-point bending

In this section, we revisit the three-point bending beam in Fig. 4(a) while prescribing a large pre-crack, as shown in Fig. 6(a). To perform topology optimization, we discretize the design domain with an unstructured mesh consisting of 107,200 first-order quadrilateral elements of average size $h = 0.05$ mm. For both the stress-constrained and fracture-based formulations, we adopt a volume fraction of $V^* = 0.45$ and a filter radius of $R = 1.5$ mm. After topology optimization, we perform the fracture analysis described in (2)–(3) for all optimized designs based on body-fitted meshes.

The optimized designs, strength surface indicators, and fracture paths are shown in Fig. 6(b). Similar to Fig. 4(b), we present a stiffness-maximization design (labeled as `stiffness`) as a reference. We also present one stress-constrained design (labeled as `stress`) with a target fracture displacement of $u_a = 1.6$ mm. Additionally, we present two fracture-based designs: `fracture 1`, corresponding to the multi-objective formulation in (16), and `fracture 2`, corresponding to the modified formulation in (18), which takes a similar form to the stress-constrained formulation in (13). Both `fracture 1` and `fracture 2` use the same critical displacement of $u_n = 1.6$ mm.

Based on Fig. 6(b), the `stiffness` design retains the pre-crack, whereas both the `stress` and `fracture 1` designs replace the pre-existing crack with a smooth boundary to delay fracture nucleation through different mechanisms. In the `stress` design, the

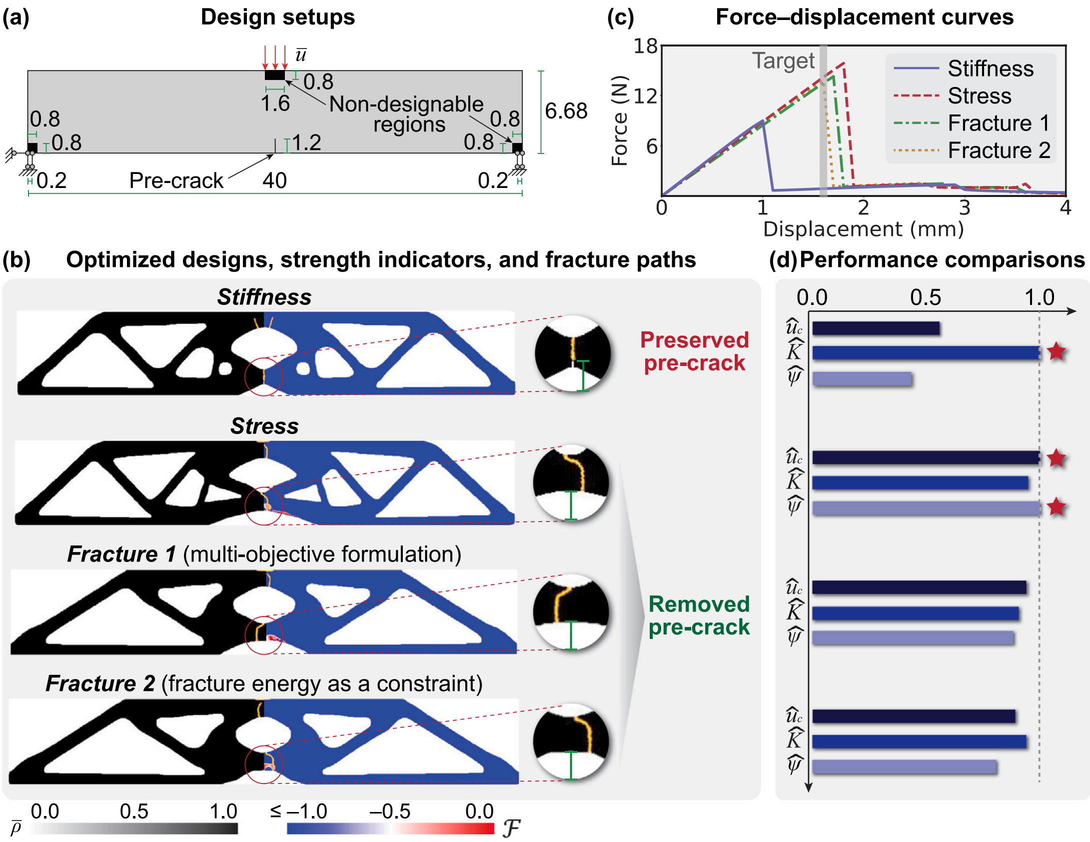

Fig. 6. Comparison among the optimized stiffness, stress, and fracture designs for a notched beam under three-point bending. (a) Design setup including the design domain and boundary conditions. The geometries are in a unit of mm. The variable $\bar{u}$ is the amplitude of the applied displacement ($\bar{\mathbf{u}}$). (b) Optimized designs ($\bar{\rho}$), strength surface indicators ($\mathcal{F}$), and fracture paths. The strength surface indicators are plotted for $\mathcal{F} \in [-1, 0]$ MPa at the load step immediately preceding the first fracture propagation, while the fracture paths are depicted at the final load step and determined using the phase-field fracture theory in (2)–(3). (c) Force–displacement (F–$\bar{u}$) responses of the optimized designs. (d) Comparisons of the normalized performance measurements, $\hat{u}_c = u_c / \max(u_c)$, $\hat{K} = K / \max(K)$, and $\hat{\Psi} = \Psi / \max(\Psi)$.

pre-crack induces stress concentration around the crack tip (e.g., Fig. 3(c)), causing the stress state to exceed the strength surface ($\mathcal{F} = 0$). To satisfy the stress constraint, the `stress` design replaces the pre-crack with rounded corners, dispersing stress and reducing stress amplitudes to delay fracture onset. Conversely, in the `fracture 1` design, the pre-crack readily triggers fracture propagation based on Griffith's energy competition, leading to a nonzero integrated fracture energy (Π_f in (17)). The `fracture 1` design minimizes Π_f through the multi-objective function in (16) by enforcing $v_0(\mathbf{X}) = v_1(\mathbf{X}) = \cdots = v_n(\mathbf{X}) \equiv 1$, which in turn implies no fracture propagation and then the removal of the pre-crack. Beyond the removal of the pre-crack, we observe that the `fracture 1` and `fracture 2` designs are nearly identical. This agreement suggests that both fracture formulations in (16) and (18) yield comparable optimized structural performance.

To quantitatively compare the responses of the optimized designs, we present their force–displacement (F–$\bar{u}$) curves in Fig. 6(c) and normalized performance indicators ($\hat{u}_c = u_c / \max(u_c)$, $\hat{K} = K / \max(K)$, and $\hat{\Psi} = \Psi / \max(\Psi)$) in Fig. 6(d). Compared to the `stiffness` design with a critical displacement of $u_c = 1.0$ mm, all of the stress-constrained and fracture-based designs effectively delay fracture nucleation, meeting the target value of 1.6 mm. Furthermore, stress-constrained and fracture-based designs exhibit comparable performance in terms of u_c, K, and Ψ, with the stress-constrained design slightly outperforming fracture designs. Therefore, we conclude that for design domains with pre-existing cracks, where enhanced toughness is primarily achieved through delaying fracture nucleation, both formulations produce optimized designs with comparable performance, albeit through different mechanisms.

4.2. T-shaped corbels with equal and unequal strengths

After analyzing the three-point bending beams, we now compare the stress-constrained and fracture-based formulations on another benchmark design domain: T-shaped corbels [23] with equal and unequal tensile–compressive ($\sigma_{\mathtt{ts}}$–$\sigma_{\mathtt{cs}}$) strengths. These examples are representative because they feature fracture nucleation from sharp corners. Additionally, through these examples, we highlight the consideration of fracture propagation in the fracture-based formulation.

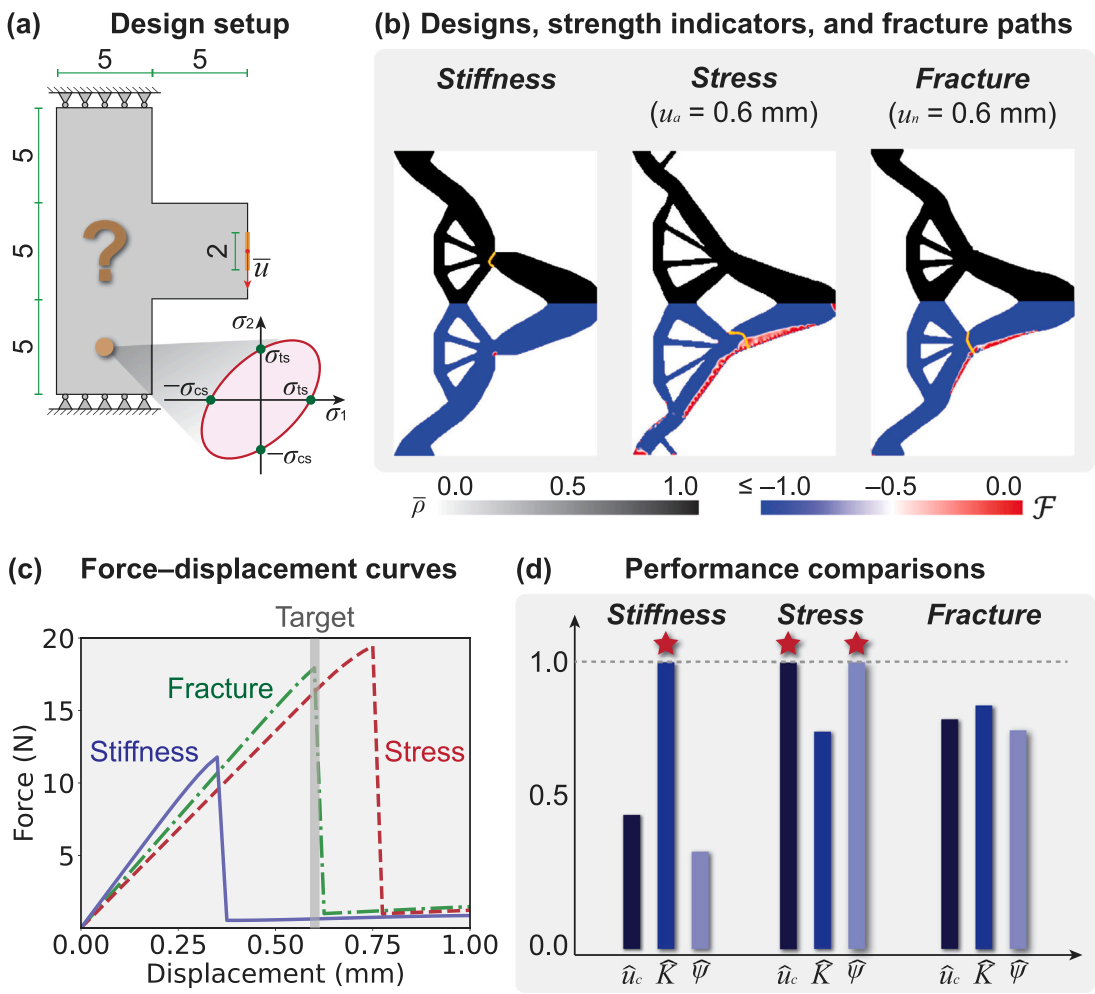

Fig. 7. Comparison among the optimized stiffness, stress, and fracture designs for a T-shaped corbel with equal tensile (σ_{ts}) and compressive (σ_{cs}) strengths. (a) Design setup including the design domain and boundary conditions. The geometries are in a unit of mm. The variable $\bar{u}$ is the amplitude of the applied displacement ($\bar{\mathbf{u}}$). The variables σ_1 and σ_2 are the principal stresses. (b) Optimized designs ($\bar{\rho}$), strength surface indicators ($\mathcal{F}$), and fracture paths. The strength surface indicators are plotted for $\mathcal{F} \in [-1, 0]$ MPa at the load step immediately preceding the first fracture propagation, while the fracture paths are depicted at the final load step and determined using the phase-field fracture theory in (2)–(3). (c) Force–displacement (F–$\bar{u}$) responses of the optimized designs. (d) Comparisons of the normalized performance measurements, $\hat{u}_c = u_c / \max(u_c)$, $\hat{K} = K / \max(K)$, and $\hat{\Psi} = \Psi / \max(\Psi)$.

4.2.1. *Corbel with equal tensile and compressive strengths*

We begin by considering a T-shaped corbel with equal tensile (σ_{ts}) and compressive (σ_{cs}) strengths. As shown in Fig. 7(a), we clamp the top and bottom edges of the corbel and apply a downward displacement loading ($\bar{u}$) in the middle of the right edge. The material inputs are the same as those in Table 4 except that here we use $\sigma_{cs} = \sigma_{ts} = 27$ MPa, which reduces the Drucker–Prager strength surface in (5) to a von Mises strength surface as

$$\mathcal{F}^{\mathrm{vm}}(J_2) = \sqrt{J_2} - \frac{\sigma_{ts}}{\sqrt{3}} = 0 \quad \text{and} \quad \Lambda(J_{2,0}) := \frac{\sqrt{3J_{2,0}}}{\sigma_{ts,0}} - 1. \tag{19}$$

Correspondingly, the δ^ε parameter used in $(3)_1$ is re-calibrated to 2.43. To perform topology optimization, we discretize the design domain with a structured mesh consisting of 40,000 first-order quadrilateral elements. For both the stress-constrained and fracture-based formulations, we adopt an allowable volume fraction of $V^* = 0.4$ and a filter radius of $R = 0.25$ mm. After topology optimization, we perform the fracture analysis based on (2)–(3) for all optimized designs with body-fitted meshes.

The optimized designs, strength surface indicators, and fracture paths are shown in Fig. 7(b). We present one stress-constrained design (`stress`) with a target fracture displacement of $u_a = 0.6$ mm and one fracture-based design (`fracture`) with a critical displacement of $u_n = 0.6$ mm. We also present a stiffness-maximization design (`stiffness`) as a reference. In both `stress` and `fracture` designs, the sharp corners are replaced with smooth boundaries through different mechanisms — the `stress` design detects the stress concentration, while the `fracture` design senses Griffith's competition of energies and its interaction with the strength criterion [56]. In contrast, the `stiffness` design retains the two sharp corners.

To quantitatively compare these optimized designs, we present the force–displacement (F–$\bar{u}$) responses in Fig. 7(c) and the normalized performance indicators ($\hat{u}_c = u_c / \max(u_c)$, $\hat{K} = K / \max(K)$, and $\hat{\Psi} = \Psi / \max(\Psi)$) in Fig. 7(d). Compared to the `stiffness` design, both the `stress` and `fracture` designs successfully delay fracture nucleation to the target value of 0.6 mm while maintaining sufficient initial stiffness. The `stress` design shows a larger failure displacement by slightly sacrificing initial stiffness. Due to the delayed fracture nucleation and sufficient initial stiffness, both `stress` and `fracture` designs exhibit improvements in effective toughness ($\Psi = 8.1$ N mm and $\Psi = 6.2$ N mm, respectively) compared to the `stiffness` design ($\Psi = 2.7$ N mm). Therefore, both stress-constrained and fracture-based formulations are effective in delaying fracture nucleation for design domains with sharp corners.

4.2.2. Corbel with unequal tensile and compressive strengths

We revisit the same corbel depicted in Fig. 7(a), but now with distinct tensile and compressive strengths as specified in Table 4 and illustrated in Fig. 8(a). We maintain all configurations from Section 4.2.1 for topology optimization, adjusting only the target fracture displacement (u_a) for stress-constrained designs and the critical displacement (u_n) for fracture-based designs. Following topology optimization, we conduct phase-field fracture analysis with (2)–(3) for all optimized designs based on body-fitted meshes.

The optimized designs alongside their fracture paths are illustrated in Fig. 8(b). It includes one stiffness-maximization design (`stiffness`) for reference and a stress-constrained design (`stress`) with a target fracture displacement of $u_a = 0.7$ mm. Additionally, three fracture-based designs are shown: `fracture 1` with $u_n = 0.7$ mm and $\omega_w = 0$ (similar to the stress-constrained setup), `fracture 2` with $u_n = 0.9$ mm and $\omega_w = 0$, and `fracture 3` with $u_n = 0.6$ mm and $\omega_w = 0.2$. For the `fracture 3` design, an applied displacement of $\bar{u} = 1.0$ mm, greater than $u_n = 0.6$ mm, is set to evaluate its post-fracture toughness during topology optimization.

The observations are as follows. Compared to the `stiffness` design, both the `stress` and `fracture 1` designs deviate from plane symmetry to take advantage of higher compressive strength (σ_{cs}) and delay structural failure. Additionally, the `stress` and `fracture 1` designs smooth the top sharp corner to reduce tensile stress, while maintaining the sharp corner at the bottom due to the redundancy in compressive strength. For a larger target failure displacement of 0.9 mm, the fracture-based approach still generates a viable design (`fracture 2`), whereas the stress-constrained method fails to converge due to an underestimation of structural fracture resistance. Notably, by optimizing for post-fracture toughness with a nonzero ω_w, the `fracture 3` design forms a porous structure similar to that in [90], exhibiting sequential fracture nucleations and propagation.

Beyond the fracture paths, we present the strength surface indicators of the optimized designs in Fig. 8(c). The stiffness design exhibits concentrated stress around the top sharp corner, whereas all stress-constrained and fracture-based designs effectively disperse the stress concentration. This dispersed stress distribution helps delay fracture nucleation. It is because fracture nucleation occurs either at sharp corners or smooth boundaries (Fig. 8(b)), which is governed by both the strength criteria and Griffith's energy competition [56].

To quantitatively compare the optimized designs in Fig. 8(b), we present their force–displacement (F–$\bar{u}$) curves and normalized performance indicators ($\hat{u}_c = u_c / \max(u_c)$, $\hat{K} = K / \max(K)$, $\hat{\Psi} = \Psi / \max(\Psi)$, and $\hat{\Psi}_l = \Psi_l / \max(\Psi_l)$) in Fig. 8(d). We observe that the `stress` and `fracture 1` designs exhibit similar performance, delaying failure displacement to the target value of 0.7 mm while maintaining sufficient initial stiffness compared to the `stiffness` design. Additionally, the `fracture 2` design further postpones failure displacement to 0.9 mm, albeit with a slight sacrifice in initial stiffness. Interestingly, the `fracture 3` design shows a plateau after initial fracture nucleation, achieved by multiple drops due to fracture re-nucleation (Fig. 8(e)). In contrast to the catastrophic failure observed in other designs, the `fracture 3` design demonstrates the highest post-fracture effective toughness (Ψ_l), despite the inherent brittleness of the used materials.

In summary, for design domains featuring sharp corners prone to fracture nucleation, both stress-constrained and fracture-based formulations produce optimized designs with comparable performance when targeting relatively small failure displacements (0.7 mm in this study). However, for the requirement of larger failure displacements (0.9 mm) with constrained material usage or when emphasizing post-fracture effective toughness, the fracture-based approach is recommended.

4.3. Unnotched and notched columns under vertical loadings

In this section, we compare stress-constrained and fracture-based formulations for both unnotched and notched columns. In the unnotched column, fracture nucleation originates from the bulk of the material, whereas in the notched column, it initiates from pre-existing defects. These two cases illustrate that the two formulations are equivalent when fracture failure is solely governed by material strength. However, when other factors come into play, the fracture-based formulation offers superior post-crack toughness. Detailed results and analyses are provided below.

4.3.1. Unnotched column under uniaxial tension

We begin by analyzing the unnotched column in Fig. 9(a). This design domain is subjected to uniaxial tension with an applied displacement of $\bar{u}$. It consists of an intact region with a tensile strength of $\sigma_{\mathrm{ts}} = 27$ MPa and a damaged region in the center with a reduced tensile strength of $\hat{\sigma}_{\mathrm{ts}} = 10$ MPa (the δ^{ε} parameter is calibrated to 7.42). For the topology optimization, the design domain is discretized using a structured mesh comprising 40,000 first-order quadrilateral elements of size $h = 0.05$ mm. Both the stress-constrained and fracture-based formulations employ a target volume fraction of $V^* = 0.4$ and a filter radius of $R = 0.3$ mm. A non-uniform initial guess (Fig. 9(b)) is used in both formulations to "mislead" them to direct more material toward the damaged

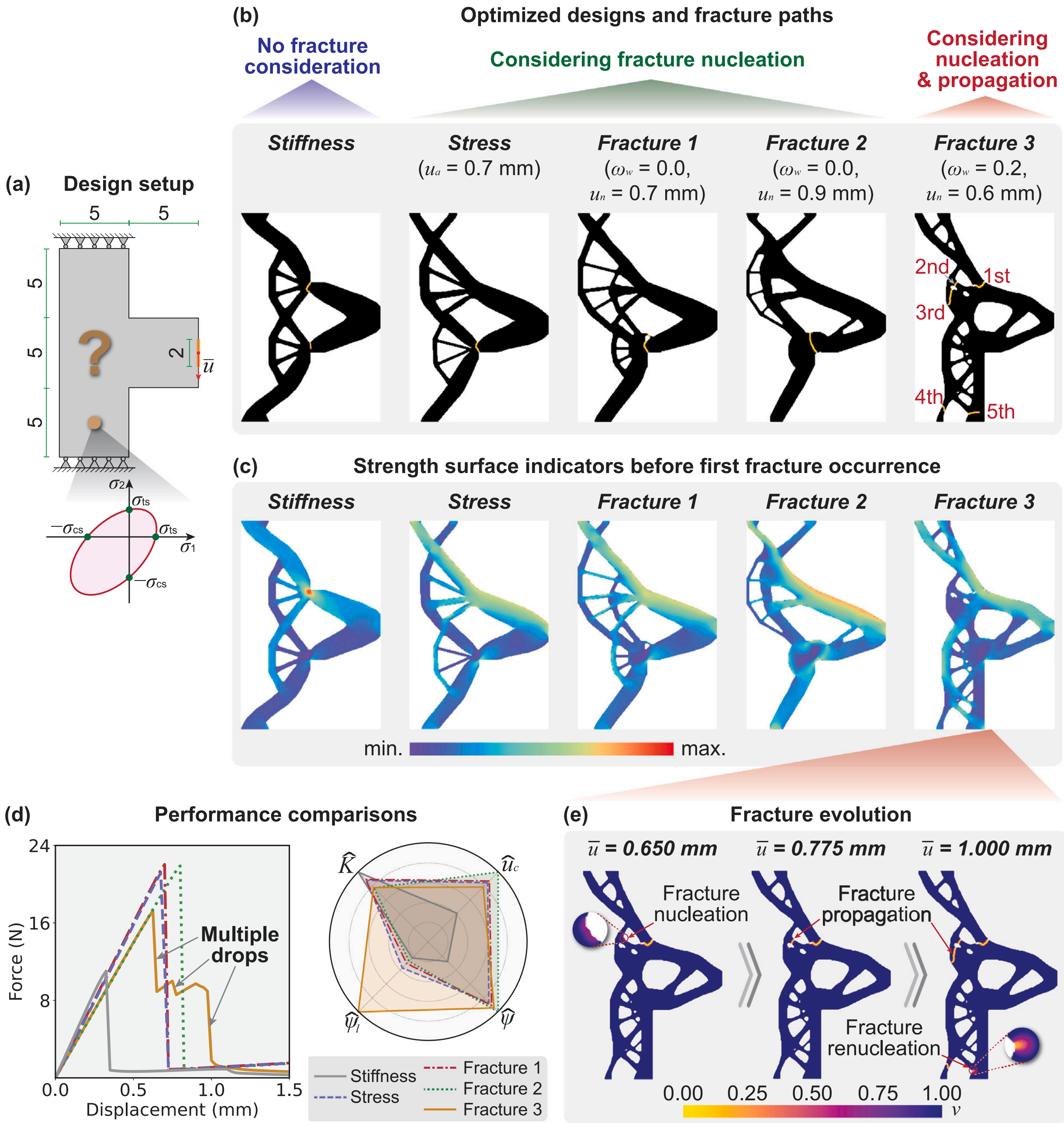

Fig. 8. Comparison among the optimized stiffness, stress, and fracture designs for a T-shaped corbel with unequal tensile (σ_{ts}) and compressive (σ_{cs}) strengths. (a) Design setup including the design domain and boundary conditions. The geometries are in a unit of mm. The variable $\bar{u}$ is the amplitude of the applied displacement ($\bar{\mathbf{u}}$). The variables σ_1 and σ_2 are the principal stresses. (b) Optimized designs and their fracture paths evaluated with the phase-field fracture theory in (2)–(3). (c) Strength surface indicators ($\mathcal{F}$) of the optimized designs. The strength surface indicators are plotted for the load step immediately preceding the first fracture propagation, and the scalar bar range corresponds to the minimum and maximum $\mathcal{F}$ value for each design. (d) Force–displacement (F–$\bar{u}$) responses of the optimized designs and the comparisons of the normalized performance measurements, $\hat{u}_c = u_c/\max(u_c)$, $\hat{K} = K/\max(K)$, $\hat{\Psi} = \Psi/\max(\Psi)$, and $\hat{\Psi}_l = \Psi_l/\max(\Psi_l)$. (e) Fracture nucleation and propagation in the `fracture 3` design in (c). The variable $v \in [0, 1]$ is the phase field.

region. Following topology optimization, a fracture analysis is performed with (2)–(3) on all optimized designs using body-fitted meshes.

The optimized designs and their corresponding fracture paths are shown in Fig. 9(c). For reference, we include one stiffness-maximization design (`stiffness`) that concentrates all material around the damaged region, where fracture nucleates and propagates. This design is misled by the non-uniform initial guess in Fig. 9(b) due to the absence of strength information. By setting u_n = 0.25 mm for the fracture-based formulation and u_a = 0.25 mm for the stress-constrained formulation, both produce

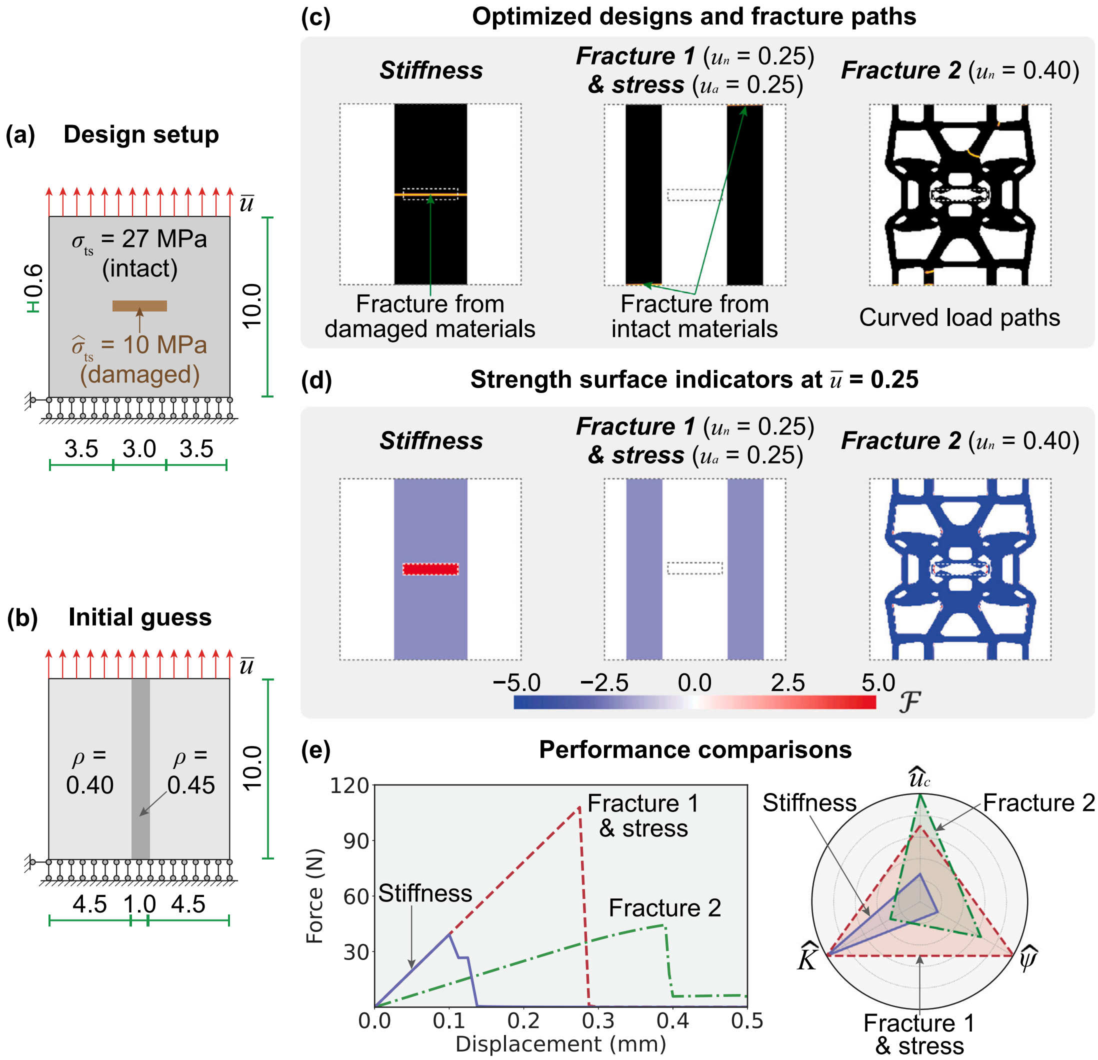

Fig. 9. Comparison among the optimized stiffness, stress, and fracture designs for an unnotched column. (a) Design setup including the design domain and boundary conditions. The design domain consists of an intact region with a tensile strength of $\sigma_{ts} = 27$ MPa and a damaged region with a tensile strength of $\hat{\sigma}_{ts} = 10$ MPa. The geometries of the design domain are in a unit of mm. The variable $\bar{u}$ is the amplitude of the applied displacement $(\bar{\mathbf{u}})$. (b) Non-uniform initial guess of the topology optimization problem. (c) Optimized designs and their fracture paths evaluated with the phase-field fracture theory in (2)–(3). The target fracture displacements u_n and u_a are measured in mm. (d) Strength surface indicators ($\mathcal{F}$) of optimized designs at $\bar{u} = 0.25$ mm based on the elastostatics (no fracture analysis). The value of $\mathcal{F}$ is limited to $[-5, 5]$ MPa for better visualization. (e) Force–displacement (F–$\bar{u}$) responses of the optimized designs and the comparisons of the normalized performance measurements, $\hat{u}_c = u_c/\max(u_c)$, and $\hat{K} = K/\max(K)$, and $\hat{\Psi} = \Psi/\max(\Psi)$.

identical optimized designs — `fracture 1` and `stress`, respectively. These designs appear as separate columns that successfully circumvent the damaged regions in contrast to `stiffness`. When u_n is increased from 0.25 mm to 0.40 mm, the fracture-based formulation results in the `fracture 2` design, which features curved load paths. However, the stress-constrained formulation fails again to generate a converged design for $u_a = 0.40$ mm, likely due to the applied displacement being too large for the formulation's restrictive stress constraints and the imposition of the volume constraint.

To explain the performance differences among the optimized designs, we plot the strength surface indicators ($\mathcal{F}$) at $\bar{u} = 0.25$ mm in Fig. 9(d) based on elastostatics (without fracture analysis). The `stiffness` design exhibits a severe violation of the strength surface ($\mathcal{F} > 0$) in the middle attributed to the damaged material, which leads to premature structural failure. In contrast, both the `fracture 1` and `stress` designs effectively circumvent the damaged material and do not violate the strength surface at $\bar{u} = 0.25$ mm, allowing for delayed fracture onset. As for the `fracture 2` design, the majority of materials satisfy the strength surface condition ($\mathcal{F} \leq 0$). Although some scattered material points violate the strength surface, they do not induce fracture nucleation due to the non-uniform stress states.

To gain deeper insights into these optimized designs, we plot their force–displacement curves and compare normalized performance metrics ($\hat{u}_c = u_c/\max(u_c)$, $\hat{K} = K/\max(K)$, and $\hat{\Psi} = \Psi/\max(\Psi)$) in Fig. 9(e). The `stiffness` design fractures prematurely at $\bar{u} = 0.100$ mm, while the `fracture 1` (`stress`) design delays fracture until $\bar{u} = 0.275$ mm (175% improvement) while maintaining the *same* stiffness of $K = 392$ N/mm. This improvement occurs because the target fracture displacement — $u_n = 0.25$ mm for `fracture 1` and $u_a = 0.25$ mm for `stress` — remains below the theoretical threshold of

$$\bar{u} = \frac{\sigma_{\mathtt{ts}} l_y}{E} = 0.275 \text{ mm}$$

for an intact column (or separate intact columns) of arbitrary widths with height l_y under uniaxial tension. In this scenario, fracture nucleation is solely controlled by material strength. Consequently, for an applied displacement $\bar{u} < 0.275$ mm, both the stress-constrained and fracture-based formulations produce identical columns that achieve the same stiffness as the `stiffness` design. For $\bar{u} > 0.275$ mm, optimized designs like `fracture 2` need to develop curved load paths to reduce stiffness and delay fracture, which becomes controlled by both strength and the critical energy release rate. Therefore, only the fracture-based formulation generates a converged design for $u_n = 0.4$ mm.

From this example, we conclude that the stress-constrained and fracture-based formulations are equivalent when fracture nucleation is controlled solely by strength, as in columns under uniaxial tension with sufficiently small applied displacement. Otherwise, the fracture-based formulation provides a more reliable design.

4.3.2. Notched column under mode I loading

In our final example, we compare the stress-constrained and fracture-based formulations for a pre-notched column, as shown in Fig. 10(a). The column is partially fixed on the left side and subjected to Mode I loading with an applied displacement amplitude of $\bar{u}$. For topology optimization, the design domain is discretized using an unstructured mesh of 24,500 first-order quadrilateral elements with an average size of $h = 0.05$ mm. Both the stress-constrained and fracture-based formulations employ a target volume fraction of $V^* = 0.8$ and a filter radius of $R = 0.6$ mm. Additionally, the initial guess (Fig. 10(b)) includes triangular voids inspired by [1]. After topology optimization, a fracture analysis is conducted with (2)–(3) on all optimized designs using body-fitted meshes.

In this example, we aim to generate fracture-resistant structures with maximum effective toughness. For the fracture-based formulation, we set a critical displacement of $u_n = 0.05$ mm. During topology optimization, we use an applied displacement of $\bar{u} = 1.50 > 0.05$ mm and a non-zero value of $\omega_w = 0.25$ to access and maximize structural toughness. For the stress-constrained formulation, we generate a series of designs with target fracture displacements of $u_a \in \{0.05, 0.10, 0.15, 0.20, 0.25\}$ mm and select one converged design that exhibits the highest product of initial stiffness (K) and target fracture displacement (u_a).

The force–displacement curves of optimized designs are shown in Fig. 10(c). We analyze one `stress` and one `fracture` design, along with a stiffness-maximization design (`stiffness`) for reference. The `stiffness` and `fracture` designs exhibit comparable initial stiffness values ($K = 108.3$ N/mm and $K = 84.7$ N/mm, respectively) and the same fracture displacement ($u_c = 0.2$ mm). In contrast, the `stress` design has a lower initial stiffness ($K = 53.0$ N/mm) but achieves a higher fracture displacement ($u_c = 0.3$ mm). Additionally, the `stress` design fails immediately after fracture nucleation, exhibiting minimal post-crack toughness ($\Psi_l = 1.3$ N mm) and total toughness ($\Psi = 3.6$ N mm). In contrast, the `stiffness` design demonstrates unexpectedly higher post-crack toughness ($\Psi_l = 6.2$ N mm) and total toughness ($\Psi = 8.1$ N mm). The `fracture` design, as expected, displays the highest post-crack toughness ($\Psi_l = 8.9$ N mm) and total toughness ($\Psi = 10.5$ N mm).

To understand these differences in performance, we plot the optimized designs in Fig. 10(d) and their phase-field predictions at the final load step in Fig. 10(e). The `stress` design replaces the pre-existing notch with a round hole, reducing stress concentration and delaying fracture nucleation. As loading increases, the fracture nucleates from the round hole and deflects toward the top edge, resulting in the shortest crack length ($l_c = 2.2$ mm) among the three designs. In contrast, the `fracture` design retains the notch tip, thereby promoting fracture nucleation and propagation, ultimately producing the longest crack, which traverses nearly the entire structure. This seemingly counterintuitive fracture promotion occurs because both post-crack toughness (Ψ_l) and total toughness (Ψ) are positively correlated with fracture propagation energy, which in return scales with crack length. As a result, the fracture-based formulation maximizes Ψ_l and Ψ by promoting a longer fracture path in the optimized design. The `stiffness` design, on the other hand, concentrates material near the loading area to create the shortest load paths and maximize initial stiffness. It retains the entire pre-notch due to the lack of strength and critical energy release rate information. Interestingly, this retained pre-notch leads to a moderately long crack length of $l_c = 6.9$ mm, giving the `stiffness` design higher Ψ_l and Ψ values than the `stress` design (Fig. 10(f)).

This example reinforces the conclusion that the fracture-based formulation is preferable when post-crack toughness (Ψ_l) and/or total toughness (Ψ) are critical. The fracture-based formulation leverages the critical energy release rate (G_c), which governs fracture propagation energy and, consequently, post-crack and total toughness. Additionally, we highlight that, in contrast to encouraging multiple fracture re-nucleations (such as `fracture 3` in Fig. 8(b)), promoting fracture propagation of a single crack (such as `fracture` in Fig. 10(d)) is also effective in maximizing structural toughness.

5. Final comments

Ever since the invention of topology optimization, stress-constrained and fracture-based formulations have become popular and effective approaches for optimizing the fracture resistance of structures. However, the applicability to different design scenarios remains unclear — particularly regarding the necessity of the complex and computationally expensive fracture-based formulation.

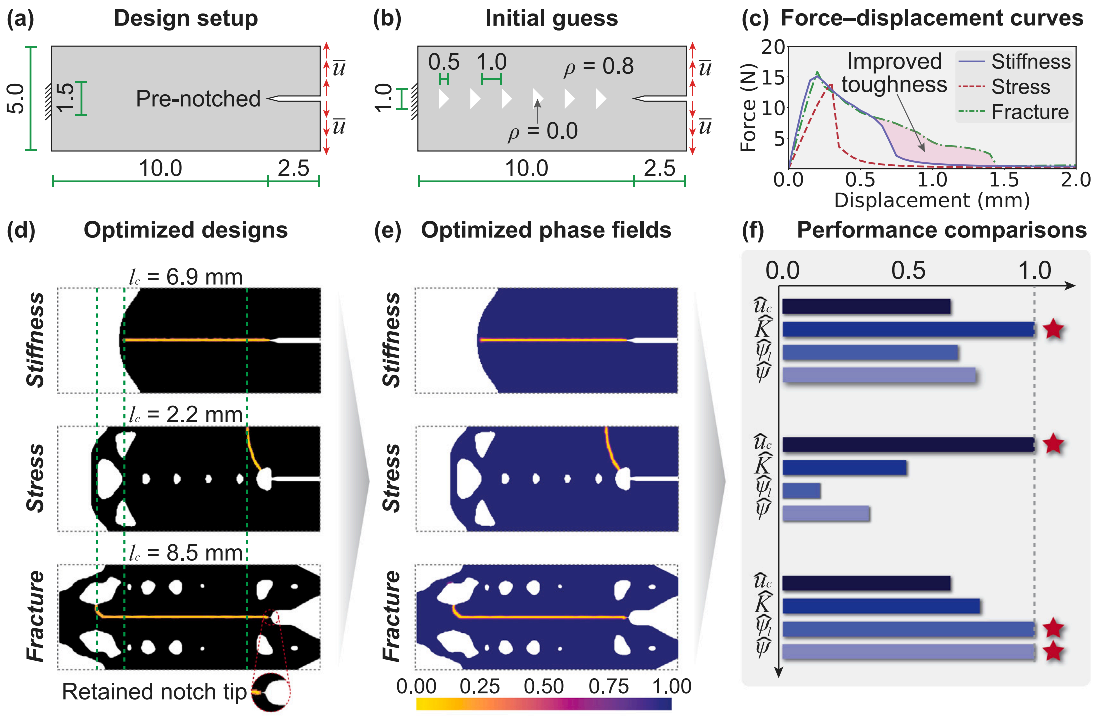

Fig. 10. Comparison among the optimized stiffness, stress, and fracture designs for a notched column. (a) Design setup including the design domain and boundary conditions. The design domain is pre-notched, and its geometries are in a unit of mm. The variable $\overline{u}$ is the amplitude of the applied displacement $(\overline{\mathbf{u}})$. (b) Non-uniform initial guess of the topology optimization problem. (c) Force–displacement (F–$\overline{u}$) responses of the optimized designs. (d) Optimized designs and fracture paths evaluated with the phase-field fracture theory in (2)–(3). The variable l_c is the crack length, and the crack tips are marked by the green dashed lines. (e) Phase fields evaluated with (2)–(3). (f) Comparisons of the normalized performance measurements, $\hat{u}_c = u_c / \max(u_c)$, $\hat{K} = K / \max(K)$, $\hat{\Psi}_l = \Psi_l / \max(\Psi_l)$, and $\hat{\Psi} = \Psi / \max(\Psi)$.

This work revisits the stress-constrained and fracture-based formulations and comprehensively examines their underlying physics and functionalities. We demonstrate that the underlying physics of both approaches predicts similar fracture nucleation for specimens under uniform stress states (Table 2), while the elastostatics applied in the stress-constrained formulation greatly underestimate the fracture resistance of cracked specimens (Table 3).

To highlight the impact of differing underlying physics on topology optimization, we systematically compare the two formulations by examining their optimized designs in six representative design setups: three-point bending beams with and without pre-cracks, T-shaped corbels with equal and unequal tensile–compressive strengths, and notched and unnotched columns under vertical loadings. Through these comparisons, we provide insights on when and why one should use a specific formulation for a given design domain, boundary condition, and design objective. Below are the conclusions:

(i) For design domains where fracture nucleates in the bulk under uniform stress states controlled by the material's strength surface ($\mathcal{F} = 0$), both formulations work effectively and yield similar optimized designs, albeit through different mechanisms. The stress-constrained formulation uses an explicitly defined strength surface in (5), while the fracture-based formulation employs an implicit yet equivalent (when $\varepsilon \searrow 0$) strength surface in (7).

(ii) For design domains where fracture nucleates from large pre-existing cracks governed by Griffith's energy competition, the fracture-based formulation should be used to accurately predict the failure displacement. However, when the applied loading is moderately large, the stress-based formulation can detect the stress concentration and remove the large existing cracks.

(iii) For design domains where fracture nucleates in other scenarios — such as in the bulk with non-uniform stress states, from small pre-existing cracks, or from smooth or sharp boundary points — controlled by the interaction of strength surface and Griffith's energy competition, the fracture-based formulation offers higher accuracy, while the stress-based formulation is recommended for higher computational efficiency.

(iv) For design objectives involving post-fracture toughness and fracture propagation, the fracture-based formulation should be used to account for fracture re-nucleation and propagation.

Despite these conclusions, it is essential to note that the fracture-based formulation in (16) addresses brittle fracture resistance, while the stress-constrained formulation in (13) enhances the structural resistance to general stress-dependent failures beyond brittle fracture (e.g., plasticity). Additionally, the stress-constrained formulation is simpler and computationally efficient, whereas the fracture-based formulation necessitates a nonlinear, strongly coupled-field fracture analysis. Therefore, the fracture-based formulation faces a significant computational bottleneck in design scenarios involving intricate three-dimensional structures and multiple load cases. Practically, one can choose to utilize both formulations synergistically to balance accuracy and efficiency. For instance, the optimized design from stress-constrained optimization can be used as the initial guess for subsequent fracture-based optimization. Alternatively, one can perform stress-constrained topology optimization (for design domains with relatively uniform stress states) and then verify the optimized design through fracture analysis.

We also note that while the comparisons in this study primarily focus on isotropic linear elastic brittle materials governed by the Drucker–Prager (Eq. (5)) and von Mises (Eq. (19)) strength surfaces, the conclusions largely extend to anisotropic materials and other strength criteria. This generality arises because the stress-constrained and fracture-based formulations examined here inherently accommodate any strength surface through a general form ($\mathcal{F} = 0$), representing a wide range of isotropic [20] and anisotropic [91] material types. Additionally, the key findings are primarily driven by the fact that, regardless of material anisotropy or the chosen strength criterion, the phase-field fracture theory [56] predicts the same failure surface as the strength theory under uniform stress states and as $\varepsilon \searrow 0$, while also utilizing G_c information to accurately predict fracture nucleation from large pre-existing cracks and the subsequent fracture propagation. However, beyond the elastic regime, the comparison between stress-constrained and ductile-fracture-based [92] (or even purely plasticity-based [26,93]) topology optimization remains an open problem that merits further exploration.

CRediT authorship contribution statement

Yingqi Jia: Writing – review & editing, Writing – original draft, Visualization, Software, Methodology, Investigation, Formal analysis, Data curation, Conceptualization. **Rahul Dev Kundu:** Writing – review & editing, Writing – original draft, Software, Methodology, Investigation. **Xiaojia Shelly Zhang:** Writing – review & editing, Writing – original draft, Supervision, Project administration, Methodology, Investigation, Funding acquisition, Conceptualization.

Declaration of competing interest

The authors declare that they have no known competing financial interests or personal relationships that could have appeared to influence the work reported in this paper.

Acknowledgments

Authors X.S.Z., Y.J., and R.D.K would like to acknowledge the support from the U.S. Defense Advanced Research Projects Agency (DARPA) Award HR0011-24-2-0333. This material is based upon work supported by the Air Force Office of Scientific Research under award number FA9550-23-1-0297. The information provided in this paper is the sole opinion of the authors and does not necessarily reflect the view of the sponsoring agencies.

Appendix A. Strength-based critical applied traction for cracked specimen

In this section, we derive the critical applied traction for cracked specimens based on the strength criterion in (5). For a specimen with a large pre-existing crack (e.g., Fig. 3(a)), the stress components at a material point (r, θ) around the crack tip (set as the origin of a polar coordinate system) can be computed as

$$\begin{cases} \sigma_{11} = \dfrac{K}{\sqrt{2\pi r}} \cos\dfrac{\theta}{2}\left(1 - \sin\dfrac{\theta}{2}\sin\dfrac{3\theta}{2}\right) \\ \sigma_{22} = \dfrac{K}{\sqrt{2\pi r}} \cos\dfrac{\theta}{2}\left(1 + \sin\dfrac{\theta}{2}\sin\dfrac{3\theta}{2}\right) \\ \sigma_{12} = \dfrac{K}{\sqrt{2\pi r}} \cos\dfrac{\theta}{2}\sin\dfrac{\theta}{2}\cos\dfrac{3\theta}{2} \end{cases} \tag{A.1}$$

where $K = \sigma\sqrt{\pi a}Y$ is the stress intensity factor depending on the applied stress (σ), half crack length (a), and specimen geometry (Y). Under the plane stress assumption, we can compute the stress invariants I_1 and J_2 near the crack tip as

$$I_1 = \frac{2K}{\sqrt{2\pi r}}\cos\frac{\theta}{2} \quad \text{and} \quad J_2 = \frac{K^2}{2\pi r}\left(\frac{4}{3} - \cos^2\frac{\theta}{2}\right)\cos^2\frac{\theta}{2}.$$

Substituting I_1 and J_2 into the strength criterion in (5) derives an algebraic equation of the critical stress intensity factor (K_{cr}) as

$$\mathcal{F}(I_1, J_2) = \frac{K_{\mathrm{cr}}}{\sqrt{2\pi r}}\cos\frac{\theta}{2}\sqrt{\frac{4}{3} - \cos^2\frac{\theta}{2}} + \frac{\sigma_{\mathrm{cs}} - \sigma_{\mathrm{ts}}}{\sqrt{3}(\sigma_{\mathrm{cs}} + \sigma_{\mathrm{ts}})}\frac{2K_{\mathrm{cr}}}{\sqrt{2\pi r}}\cos\frac{\theta}{2} - \frac{2\sigma_{\mathrm{cs}}\sigma_{\mathrm{ts}}}{\sqrt{3}(\sigma_{\mathrm{cs}} + \sigma_{\mathrm{ts}})} = 0.$$

After solving for the K_{cr}, we compute the critical applied traction as

$$\bar{t}^{\mathcal{F}}_{\mathrm{cr}}(r,\theta) = \frac{K_{\mathrm{cr}}}{Y\sqrt{\pi a}} = \frac{1}{Y}\sqrt{\frac{2r}{a}}\sec\frac{\theta}{2}\,\frac{2\sigma_{\mathrm{cs}}\sigma_{\mathrm{ts}}}{\sqrt{3}(\sigma_{\mathrm{cs}}+\sigma_{\mathrm{ts}})}\left[\sqrt{\frac{4}{3}-\cos^2\frac{\theta}{2}}+\frac{2(\sigma_{\mathrm{cs}}-\sigma_{\mathrm{ts}})}{\sqrt{3}(\sigma_{\mathrm{cs}}+\sigma_{\mathrm{ts}})}\right]^{-1}. \tag{A.2}$$

Note that $\bar{t}^{\mathcal{F}}_{\mathrm{cr}}$ is a function of both r and $\cos(\theta/2)$ in the form of

$$\bar{t}^{\mathcal{F}}_{\mathrm{cr}}(r,\theta) = \frac{f(r)}{h(\cos(\theta/2))}$$

with

$$f(r) = \frac{1}{Y}\frac{2\sigma_{\mathrm{cs}}\sigma_{\mathrm{ts}}}{\sqrt{3}(\sigma_{\mathrm{cs}}+\sigma_{\mathrm{ts}})}\sqrt{\frac{2r}{a}} \quad \text{and} \quad h(\cos(\theta/2)) = \cos\frac{\theta}{2}\left[\sqrt{\frac{4}{3}-\cos^2\frac{\theta}{2}}+\frac{2(\sigma_{\mathrm{cs}}-\sigma_{\mathrm{ts}})}{\sqrt{3}(\sigma_{\mathrm{cs}}+\sigma_{\mathrm{ts}})}\right].$$

After some algebra, we can show that the maximizer of $h(\cos(\theta/2))$ and the minimizer of $\bar{t}^{\mathcal{F}}_{\mathrm{cr}}(r,\theta)$ conforms to

$$\cos\frac{\hat{\theta}}{2} = \frac{1}{2\sqrt{6}}\left(-3\gamma^2+\gamma\sqrt{9\gamma^2+96}+16\right)^{1/2} \quad \text{and} \quad \gamma = \frac{2(\sigma_{\mathrm{cs}}-\sigma_{\mathrm{ts}})}{\sqrt{3}(\sigma_{\mathrm{cs}}+\sigma_{\mathrm{ts}})}. \tag{A.3}$$

Finally, solving (A.3) for $\hat{\theta}$ and then substituting it into (A.2) renders the r-dependent strength-based critical applied traction in (8).

Appendix B. Computer algorithms of stress-constrained and fracture-based formulations

In this section, we provide the computer algorithms for implementing stress-constrained and fracture-based formulations.

B.1. Computer algorithm for the AL-based stress-constrained formulation

To enable representative stress-constrained topology optimization, we adopt the AL-based methodology in the educational paper of PolyStress [94] with the following modifications: (1) accommodating different von Mises and Drucker–Prager strength surfaces [20,23], (2) transitioning from force-loading to displacement-loading in FEA, and (3) incorporating the MMA optimizer to accommodate the volume constraint (g_2) in (13). The AL-based stress-constrained formulation is detailed below.

In the AL scheme, we sequentially solve a series of optimization subproblems to approximate the solution of the original one in (13). In subproblem i, we modify the original objective function (J) with an AL version ($\mathcal{L}^{(i)}$) defined as

$$\mathcal{L}^{(i)}\left(\bar{\rho},\mathbf{u}\right) = J\left(\bar{\rho},\mathbf{u}\right) + P^{(i)}\left(\bar{\rho},\mathbf{u}\right), \tag{B.1}$$

where $P^{(i)}$ is the augmented penalty function expressed as

$$P^{(i)}\left(\bar{\rho},\mathbf{u}\right) = \frac{1}{N^{\mathrm{elem}}}\sum_{e=1}^{N^{\mathrm{elem}}}\left\{\hat{\lambda}^{(i)}_e h_e\left(\bar{\rho},\mathbf{u}\right) + \frac{\hat{\mu}^{(i)}}{2}\left[h_e\left(\bar{\rho},\mathbf{u}\right)\right]^2\right\}. \tag{B.2}$$

Here, the parameter $\hat{\lambda}^{(i)}_e$ is the Lagrange multiplier estimator of element e in subproblem i, and $\hat{\mu}^{(i)} > 0$ is a penalty factor. The function h_e represents an equality constraint defined as

$$h_e\left(\bar{\rho},\mathbf{u}\right) = \max\left\{g_{1,e}\left(\bar{\rho},\mathbf{u}\right), -\frac{\hat{\lambda}^{(i)}_e}{\hat{\mu}^{(i)}}\right\},$$

where we recall $g_{1,e}$ is the element-wise polynomial-vanishing [20] local stress constraint in (13).

Using the solution $\bar{\rho}^{(i,*)}$ of subproblem i, we update the Lagrange multiplier estimator ($\hat{\lambda}^{(i+1)}_e$) and the penalty coefficient ($\hat{\mu}^{(i+1)}$) for subproblem $i+1$ as

$$\hat{\lambda}^{(i+1)}_e = \hat{\lambda}^{(i)}_e + \hat{\mu}^{(i)}h_e\left(\bar{\rho}^{(i,*)},\mathbf{u}\right) \quad \text{and} \quad \hat{\mu}^{(i+1)} = \max\left\{\alpha\hat{\mu}^{(i)}, \mu^{\max}\right\} \tag{B.3}$$

with some constant $\alpha > 1$ and $\mu^{\max}$ as the upper bound of $\hat{\mu}^{(i+1)}$ for numerical stability. For all examples in Section 4, we use $\hat{\lambda}^{(1)}_e = 0$, $\hat{\mu}^{(1)} = 10$, $\alpha = 1.05$, and $\mu^{\max} = 10^4$. Additionally, we allow for 5 AL iterations within each optimization subproblem. The computer algorithm for the AL-based stress-constrained formulation is presented in Algorithm 1.

B.2. Computer algorithm for the fracture-based formulation

The computational algorithm for the fracture-based topology optimization formulation in (16) is detailed in Algorithm 2, which builds upon the pseudo-code of the phase-field fracture theory presented in Algorithm 3.

Algorithm 1: Computer algorithm for the stress-constrained formulation in (13)

Inputs: maximum optimization iteration, $N^{\mathtt{opt}}$; maximum inner AL iteration, N^{AL}; number of finite elements, $N^{\mathtt{elem}}$; tolerance for updating the AL penalty parameter, $\varepsilon^{\mathrm{AL}}$; initial design variable, $\rho^{(0)}$;
Initialize the AL parameters, $\hat{\lambda}_e^{(1)} \leftarrow 0$ for $e = 1, 2, \ldots, N^{\mathtt{elem}}$ and $\hat{\mu}^{(1)} \leftarrow 10$;
Initialize the optimization iteration counter (subproblem counter), $i \leftarrow 1$;
while $i \le N^{opt}$ **do**
  Initialize the design variable of optimization iteration i and AL iteration 1, $\rho^{(i,1)} \leftarrow \rho^{(i-1)}$;
  Initialize the inner AL iteration counter, $k \leftarrow 1$;
  while $k \le N^{AL}$ **do**
    Convert the design variable ($\rho^{(i,k)}$) to the filtered design variable ($\widetilde{\rho}^{(i,k)}$) with the linear filter in (10);
    Convert the filtered design variable ($\widetilde{\rho}^{(i,k)}$) to the projected/physical design variable ($\overline{\rho}^{(i,k)}$) with the Heaviside projection in (11);
    Interpolate the material properties, $E(\overline{\rho}^{(i,k)})$ and $\nu(\overline{\rho}^{(i,k)})$, based on the physical design variable ($\overline{\rho}^{(i,k)}$) and interpolation rules in (12);
    Compute the displacement field ($\mathbf{u}^{(i,k)}$) by solving the linear elastostatics problem in (1) based on the interpolated material properties ($E(\overline{\rho}^{(i,k)})$ and $\nu(\overline{\rho}^{(i,k)})$);
    Compute the value and sensitivity of the AL penalty function ($P^{(i,k)}$) in (B.2) based on $\overline{\rho}^{(i,k)}$, $\mathbf{u}^{(i,k)}$, $\hat{\lambda}_e^{(i)}$, and $\hat{\mu}^{(i)}$;
    Compute the values and sensitivities of the objective (J) and non-stress-constraint (g_2) functions in (13);
    Add the AL penalty function ($P^{(i,k)}$) to the original objective function (J) in (B.1).
    Update the design variable ($\rho^{(i,k+1)}$) based on the function values and sensitivities as well as the MMA optimizer;
    Compute the change of the design variable, $c_\rho \leftarrow \max|\rho^{(i,k+1)} - \rho^{(i,k)}|$;
    Update the inner AL iteration counter, $k \leftarrow k + 1$;
  end
  Update the Lagrange multiplier estimator ($\hat{\lambda}_e^{(i+1)}$) based on $(\mathrm{B.3})_1$;
  if $c_\rho \le \varepsilon^{AL}$ **then**
    Update the AL penalty factor ($\hat{\mu}^{(i+1)}$) based on $(\mathrm{B.3})_2$;
  else
    Let $\hat{\mu}^{(i+1)} \leftarrow \hat{\mu}^{(i)}$;
  end
  Update the design variable, $\rho^{(i)} \leftarrow \rho^{(i,k+1)}$, of optimization iteration i;
  Update the optimization iteration counter, $i \leftarrow i + 1$;
end

Algorithm 2: Computer algorithm for the fracture-based formulation in (16)

Inputs: maximum optimization iteration, $N^{\mathtt{opt}}$;
Initialize the optimization iteration counter, $i \leftarrow 1$;
while $i \le N^{opt}$ **do**
  Convert the design variable (ρ) to the filtered design variable ($\widetilde{\rho}$) with the linear filter in (10);
  Convert the filtered design variable ($\widetilde{\rho}$) to the projected/physical design variable ($\overline{\rho}$) with the Heaviside projection in (11);
  Interpolate the fracture-related material properties, $E(\overline{\rho})$, $\nu(\overline{\rho})$, $G_c(\overline{\rho})$, $\sigma_{\mathtt{cs}}(\overline{\rho})$, and $\sigma_{\mathtt{ts}}(\overline{\rho})$, based on the physical design variable ($\overline{\rho}$) and interpolation rules in (14);
  Compute the displacement field ($\mathbf{u}$) and phase field (v) of all load steps based on the interpolated material properties ($E(\overline{\rho})$, $\nu(\overline{\rho})$, $G_c(\overline{\rho})$, $\sigma_{\mathtt{cs}}(\overline{\rho})$, and $\sigma_{\mathtt{ts}}(\overline{\rho})$) and Algorithm 3;
  Compute the values and sensitivities of the objective and constraint functions;
  Update the design variable (ρ) based on the function values and sensitivities as well as the MMA optimizer;
  Update the optimization iteration counter, $i \leftarrow i + 1$;
end

Appendix C. Stiffness maximization with nonzero Dirichlet boundary values

C.1. Maximizing versus minimizing strain energy

In this section, we explain why to maximize the strain energy (W) in (13) and (16) — instead of minimizing the strain energy like the classical "compliance minimization" formulation in [4] (note that compliance $C = 2W$ in linear elasticity) — for maximizing initial structural stiffness. We illustrate this point with a one-dimensional spring with stiffness, k. One end of the spring is fixed, and we now consider two load cases on the other end.

- Subjected to the applied force of $\overline{f} \neq 0$. The strain energy is $W = \overline{f}^2/2k$. Minimizing the strain energy gives the maximized stiffness because $k = \overline{f}^2/2W$.

Algorithm 3: Computer algorithm for the phase-field fracture problem in (2)–(3)

Inputs: maximum load step in FEA, $N^{\mathtt{step}}$; maximum stagger iteration, $N^{\mathtt{stag}} \leftarrow 100$; maximum Newton iteration, $N^{\mathtt{newton}} \leftarrow 50$; relative tolerances of displacement and phase fields of stagger iterations, $R^{\mathtt{stag,u}} \leftarrow 10^{-6}$ and $R^{\mathtt{stag,v}} \leftarrow 10^{-6}$, respectively; absolute and relative tolerances of Newton iterations, $A^{\mathtt{newton}} \leftarrow 10^{-50}$ and $R^{\mathtt{newton}} \leftarrow 10^{-8}$, respectively;
Initialize the converged displacement and phase fields at load step 0, $\mathbf{u}_0 \leftarrow \mathbf{0}$ and $v_0 \leftarrow 1$, respectively;
Initialize the load step counter, $j \leftarrow 1$;
while $j \leq N^{step}$ **do**
  Initialize the displacement and phase fields at load step j and stagger iteration 0, $\mathbf{u}_{j,0} \leftarrow \mathbf{u}_{j-1}$ and $v_{j,0} \leftarrow v_{j-1}$, respectively;
  Initialize the stagger iteration counter, $k \leftarrow 1$;
  while $k \leq N^{stag}$ **do**
    Solve for the displacement field ($\mathbf{u}_{j,k}$) at load step j and stagger iteration k from the displacement subproblem in (2) based on $v_{j,k-1}$;
    Initialize the phase field at load step j, stagger iteration k, and Newton iteration 0, $v^0_{j,k} \leftarrow v_{j,k-1}$;
    Initialize the Newton iteration counter, $l \leftarrow 1$;
    while $l \leq N^{newton}$ **do**
      Solve for the phase field increment ($\delta v^l_{j,k}$) at load step j, stagger iteration k, and Newton iteration l from the phase field subproblem in (3) based on $\mathbf{u}_{j,k}$ and $v^{l-1}_{j,k}$;
      Update the phase field at load step j, stagger iteration k, and Newton iteration l, $v^l_{j,k} \leftarrow v^{l-1}_{j,k} + \delta v^l_{j,k}$;
      Compute the absolute 2-norm of the global residual vector of (3), $a^l_{j,k}$;
      Compute the relative 2-norm of the global residual vector, $r^l_{j,k} \leftarrow a^l_{j,k}/a^1_{j,k}$;
      if $a^l_{j,k} \leq A^{newton}$ *or* $r^l_{j,k} \leq R^{newton}$ **then**
        Break the Newton iteration;
      end
      Update the Newton iteration counter, $l \leftarrow l+1$;
    end
    Record the converged phase field at load step j and stagger iteration k, $v_{j,k} \leftarrow v^l_{j,k}$;
    if $k = 1$ **then**
      Compute the absolute 2-norms of the global displacement and phase field vectors, $u^{\mathrm{norm}}_{j,1} = ||\mathbf{U}_{j,1}||_2$ and $v^{\mathrm{norm}}_{j,1} = ||\mathbf{V}_{j,1}||_2$, respectively;
      Initialize the relative 2-norms of the changes of displacement and phase fields, $r^{[u]}_{j,1} \leftarrow 1$ and $r^{[v]}_{j,1} \leftarrow 1$, respectively;
    else
      Compute the absolute 2-norms of the changes of the global displacement and phase field vectors, $\Delta u^{\mathrm{norm}}_{j,k} = ||\mathbf{U}_{j,k} - \mathbf{U}_{j,k-1}||_2$ and $\Delta v^{\mathrm{norm}}_{j,k} = ||\mathbf{V}_{j,k} - \mathbf{V}_{j,k-1}||_2$, respectively;
      Compute the relative 2-norms of the changes of displacement and phase fields, $r^{[u]}_{j,k} \leftarrow \Delta u^{\mathrm{norm}}_{j,k}/u^{\mathrm{norm}}_{j,1}$ and $r^{[v]}_{j,k} \leftarrow \Delta v^{\mathrm{norm}}_{j,k}/v^{\mathrm{norm}}_{j,1}$, respectively;
    end
    if $r^{[u]}_{j,k} \leq R^{stag,u}$ *and* $r^{[v]}_{j,k} \leq R^{stag,v}$ **then**
      Break the stagger iteration;
    end
    Update the stagger iteration counter, $k \leftarrow k+1$;
  end
  Record the converged displacement and phase fields at load step j, $\mathbf{u}_j \leftarrow \mathbf{u}_{j,k}$ and $v_j \leftarrow v_{j,k}$, respectively;
  Update the load step counter, $j \leftarrow j+1$;
end

- Subjected to the applied displacement of $\bar{u} \neq 0$. The strain energy is $W = k\bar{u}^2/2$, and maximizing the strain energy gives maximized stiffness because $k = 2W/\bar{u}^2$.

Therefore, the selection between minimizing and maximizing the strain energy/compliance for maximizing stiffness depends on boundary conditions. See the related discussion for hyperelasticity in [95].

C.2. Sensitivity analysis with nonzero Dirichlet boundary values

In this section, we derive the complete sensitivity expression of the compliance ($C = 2W$) when involving nonzero Dirichlet boundary values. Importantly, this complete sensitivity expression is different from the classical one expressed as [4]

$$\frac{\mathrm{d}C}{\mathrm{d}\rho_e} = -\mathbf{U}^\top \frac{\partial \mathbf{K}}{\partial \rho_e}\mathbf{U} \tag{C.1}$$

— no matter whether we minimize or maximize C. Here the compliance $C = \mathbf{F}^{\mathrm{int}} \cdot \mathbf{U} = \mathbf{U}^\top\mathbf{K}\mathbf{U}$. Symbols $\mathbf{K}$, $\mathbf{U}$, and $\mathbf{F}^{\mathrm{int}}$ are the global stiffness matrix, displacement vector, and *internal* force vector, respectively. The variable ρ_e is the design variable of finite element e.

Table D.6
Computational time of stress-constrained and fracture-based formulations.

Sections of examples	DOF counts	Stress-constrained		Fracture-based	
		Per iter. (s)	Total (h)	Per iter. (s)	Total (h)
Section 4.1.1	241,902	41.9	7.1 (600 iters.)	314.6 (16 cores)	52.4 (600 iters.)
Section 4.1.2	216,318	48.9	8.2 (600 iters.)	136.2 (16 cores)	22.7 (600 iters.)
Section 4.2.1	81,002	12.0	2.1 (600 iters.)	216.0 (12 cores)	36.0 (600 iters.)
Section 4.2.2	81,002	13.1	2.2 (600 iters.)	74.2 (16 cores)	12.4 (600 iters.)
Section 4.3.1	80,802	13.0	1.8 (500 iters.)	140.2 (8 cores)	19.5 (500 iters.)
Section 4.3.2	49,798	8.1	1.3 (600 iters.)	590.8 (16 cores)	98.5 (600 iters.)

We now define the global residual vector as $\mathbf{R} = \mathbf{F}^{\text{int}} - \mathbf{F}^{\text{ext}}$ with $\mathbf{F}^{\text{ext}}$ representing the global *external* force vector. Note that $\mathbf{F}^{\text{ext}}$ depends only on the applied traction ($\bar{\mathbf{t}}$) and body force ($\bar{\mathbf{b}}$), and the elements of $\mathbf{R}$ can be nonzero for fixed degrees of freedom. For clarity, we separate all global quantities based on the fixed (represented by subscript d) and free (represented by subscript f) degrees of freedom and derive

$$\mathbf{R} = \begin{bmatrix} \mathbf{R}_d \\ \mathbf{R}_f \end{bmatrix} = \begin{bmatrix} \mathbf{K}_{dd} & \mathbf{K}_{df} \\ \mathbf{K}_{fd} & \mathbf{K}_{ff} \end{bmatrix} \begin{bmatrix} \mathbf{U}_d \\ \mathbf{U}_f \end{bmatrix} - \begin{bmatrix} \mathbf{F}_d^{\text{ext}} \\ \mathbf{F}_f^{\text{ext}} \end{bmatrix}$$

where we note that $\mathbf{R}_d \neq \mathbf{0}$ and $\mathbf{R}_f = \mathbf{0}$.

Next, we construct the Lagrangian expression ($\hat{C}$) of the compliance (C) based on the adjoint method as [4]

$$\hat{C} = C + \lambda_f \cdot \mathbf{R}_f$$

where λ_f is an arbitrary adjoint vector to be determined. Taking the derivative of $\hat{C}$ with respect to ρ_e yields

$$\frac{\mathrm{d}C}{\mathrm{d}\rho_e} = \frac{\mathrm{d}\hat{C}}{\mathrm{d}\rho_e} = \frac{\partial C}{\partial \rho_e} + \frac{\partial C}{\partial \mathbf{U}_f} \cdot \frac{\partial \mathbf{U}_f}{\partial \rho_e} + \lambda_f \cdot \frac{\partial \mathbf{R}_f}{\partial \rho_e} + \left[\left(\frac{\partial \mathbf{R}_f}{\partial \mathbf{U}_f} \right)^{\top} \lambda_f \right] \cdot \frac{\partial \mathbf{U}_f}{\partial \rho_e}$$

as $\partial \mathbf{U}_d / \partial \rho_e = \mathbf{0}$. Regrouping terms gives the sensitivity as

$$\frac{\mathrm{d}C}{\mathrm{d}\rho_e} = \frac{\partial C}{\partial \rho_e} + \lambda_f \cdot \frac{\partial \mathbf{R}_f}{\partial \rho_e} + \left[\left(\frac{\partial \mathbf{R}_f}{\partial \mathbf{U}_f} \right)^{\top} \lambda_f + \frac{\partial C}{\partial \mathbf{U}_f} \right] \cdot \frac{\partial \mathbf{U}_f}{\partial \rho_e}.$$

To eliminating the expensive term, $\partial \mathbf{U}_f / \partial \rho_e$, we set

$$\left(\frac{\partial \mathbf{R}_f}{\partial \mathbf{U}_f} \right)^{\top} \lambda_f = -\frac{\partial C}{\partial \mathbf{U}_f} \quad \Rightarrow \quad \lambda_f = -2(\mathbf{K}_{ff}^{-1} \mathbf{K}_{fd} \mathbf{U}_d + \mathbf{U}_f)$$

by noticing $(\partial \mathbf{R}_f / \partial \mathbf{U}_f)^{\top} = \mathbf{K}_{ff}^{\top} = \mathbf{K}_{ff}$ and $\partial C / \partial \mathbf{U}_f = 2(\mathbf{K}_{fd} \mathbf{U}_d + \mathbf{K}_{ff} \mathbf{U}_f)$. Therefore, the complete sensitivity expression of compliance is derived as

$$\frac{\mathrm{d}C}{\mathrm{d}\rho_e} = \mathbf{U}^{\top} \frac{\partial \mathbf{K}}{\partial \rho_e} \mathbf{U} - 2(\mathbf{K}_{ff}^{-1} \mathbf{K}_{fd} \mathbf{U}_d + \mathbf{U}_f) \cdot \left(\frac{\partial \mathbf{K}_{fd}}{\partial \rho_e} \mathbf{U}_d + \frac{\partial \mathbf{K}_{ff}}{\partial \rho_e} \mathbf{U}_f \right),$$

which can be reduced to (C.1) if and only if $\mathbf{U}_d = \mathbf{0}$ — i.e., without non-zero Dirichlet boundary values. We note that the sensitivity analysis presented here pertains to elastostatics by enforcing $v \equiv 1$. For sensitivity computations involving phase-field fracture, we refer interested readers to Appendix B of [7].

Appendix D. Computational time of stress-constrained and fracture-based formulations

In this section, we compare the stress-constrained and fracture-based formulations from a computational perspective. As detailed in Section 4, the stress-constrained formulation is implemented using MATLAB, while the fracture-based formulation is implemented with FEniTop software [87]. The MATLAB implementation utilizes vectorized operations and MEX functions to accelerate computations, and the FEniTop implementation leverages the Message Passing Interface (MPI) for parallel computing. Both implementations are run on identical hardware: an AMD Ryzen Threadripper PRO 3995WX CPU with 64 physical cores and 256 GB of memory.

The computational time per optimization iteration and total runtime for both formulations are summarized in Table D.6, where we evaluate a single design case for each example and formulation. Despite differences in software environments, the fracture-based formulation typically requires 3–20 times more computational time than the stress-constrained formulation. An exception is the notched column example in Section 4.3.2, which takes 76 times longer due to early fracture nucleation and the increased number of load steps required.

The discrepancy in computational time between the two formulations arises from the fundamental differences in the underlying physics: the stress-constrained formulation solves a linear, single-field elastostatics problem in (1), while the fracture-based formulation deals with a nonlinear, strongly coupled-field fracture problem in (2)–(3). The latter requires three additional nested iterative loops (Algorithm 3) — an outer loop for load steps in the FEA, a middle staggered loop for solving the coupled fields, and an inner Newton–Raphson loop to handle the nonlinearity of the phase field subproblem in (3). Consequently, the fracture-based formulation is inherently more time-consuming and demands advanced computational techniques for acceleration, such as parallel computing, robust monolithic (rather than staggered) solvers [96], and adaptive mesh refinement [97].

Data availability

Data will be made available on request.

References

[1] N.R. Brodnik, S. Brach, C.M. Long, G. Ravichandran, B. Bourdin, K.T. Faber, K. Bhattacharya, Fracture diodes: Directional asymmetry of fracture toughness, Phys. Rev. Lett. 126 (2) (2021) 025503, http://dx.doi.org/10.1103/PhysRevLett.126.025503.

[2] T. Magrini, C. Fox, A. Wihardja, A. Kolli, C. Daraio, Control of mechanical and fracture properties in two-phase materials reinforced by continuous, irregular networks, Adv. Mater. 36 (6) (2024) 2305198, http://dx.doi.org/10.1002/adma.202305198.

[3] M.P. Bendsøe, N. Kikuchi, Generating optimal topologies in structural design using a homogenization method, Comput. Methods Appl. Mech. Engrg. 71 (2) (1988) 197–224, http://dx.doi.org/10.1016/0045-7825(88)90086-2.

[4] M.P. Bendsoe, O. Sigmund, Topology Optimization: Theory, Methods, and Applications, Springer Science & Business Media, 2003.

[5] C. Wang, Z. Zhao, M. Zhou, O. Sigmund, X.S. Zhang, A comprehensive review of educational articles on structural and multidisciplinary optimization, Struct. Multidiscip. Optim. 64 (2021) 2827–2880, http://dx.doi.org/10.1007/s00158-021-03050-7.

[6] L.L. Beghini, A. Beghini, N. Katz, W.F. Baker, G.H. Paulino, Connecting architecture and engineering through structural topology optimization, Eng. Struct. 59 (2014) 716–726, http://dx.doi.org/10.1016/j.engstruct.2013.10.032.

[7] Y. Jia, O. Lopez-Pamies, X.S. Zhang, Controlling the fracture response of structures via topology optimization: From delaying fracture nucleation to maximizing toughness, J. Mech. Phys. Solids 173 (2023) 105227, http://dx.doi.org/10.1016/j.jmps.2023.105227.

[8] W. Li, Y. Jia, F. Wang, O. Sigmund, X.S. Zhang, Programming and physical realization of extreme three-dimensional responses of metastructures under large deformations, Internat. J. Engrg. Sci. 191 (2023) 103881, http://dx.doi.org/10.1016/j.ijengsci.2023.103881.

[9] Y. Jia, K. Liu, X.S. Zhang, Topology optimization of irregular multiscale structures with tunable responses using a virtual growth rule, Comput. Methods Appl. Mech. Engrg. 425 (2024) 116864, http://dx.doi.org/10.1016/j.cma.2024.116864.

[10] Y. Jia, K. Liu, X.S. Zhang, Unstructured growth of irregular architectures for optimized metastructures, J. Mech. Phys. Solids 192 (2024) 105787, http://dx.doi.org/10.1016/j.jmps.2024.105787.

[11] N. Aage, E. Andreassen, B.S. Lazarov, O. Sigmund, Giga-voxel computational morphogenesis for structural design, Nature 550 (2017) 84–86, http://dx.doi.org/10.1038/nature23911.

[12] Y. Jia, K. Liu, X.S. Zhang, Modulate stress distribution with bio-inspired irregular architected materials towards optimal tissue support, Nat. Commun. 15 (2024) 4072, http://dx.doi.org/10.1038/s41467-024-47831-2.

[13] C. Wang, Z. Zhao, J. Han, A.A. Sharma, H. Wang, X.S. Zhang, Wireless magnetic robot for precise hierarchical control of tissue deformation, Adv. Sci. 11 (35) (2024) 2308619, http://dx.doi.org/10.1002/advs.202308619.

[14] Y. Wu, J. Yvonnet, P. Li, Z.-C. He, Topology optimization for enhanced dynamic fracture resistance of structures, Comput. Methods Appl. Mech. Engrg. 394 (2022) 114846, http://dx.doi.org/10.1016/j.cma.2022.114846.

[15] J. Zhang, F. van Keulen, A.M. Aragón, On tailoring fracture resistance of brittle structures: A level set interface-enriched topology optimization approach, Comput. Methods Appl. Mech. Engrg. 388 (2022) 114189, http://dx.doi.org/10.1016/j.cma.2021.114189.

[16] O. Giraldo-Londoño, J.B. Russ, M.A. Aguiló, G.H. Paulino, Limiting the first principal stress in topology optimization: a local and consistent approach, Struct. Multidiscip. Optim. 65 (2022) 254, http://dx.doi.org/10.1007/s00158-022-03320-y.

[17] S. Singh, L. Pflug, J. Mergheim, M. Stingl, On optimization of heterogeneous materials for enhanced resistance to bulk fracture, Forces Mech. 12 (2023) 100200, http://dx.doi.org/10.1016/j.finmec.2023.100200.

[18] J.B. Russ, G.H. Paulino, On topology optimization with gradient-enhanced damage: An alternative formulation based on linear physics, J. Mech. Phys. Solids 173 (2023) 105204, http://dx.doi.org/10.1016/j.jmps.2023.105204.

[19] M. Bruggi, On an alternative approach to stress constraints relaxation in topology optimization, Struct. Multidiscip. Optim. 36 (2008) 125–141, http://dx.doi.org/10.1007/s00158-007-0203-6.

[20] O. Giraldo-Londoño, G.H. Paulino, A unified approach for topology optimization with local stress constraints considering various failure criteria: von Mises, Drucker–Prager, Tresca, Mohr–Coulomb, Bresler–Pister and Willam–Warnke, Proc. R. Soc. A: Math. Phys. Eng. Sci. 476 (2238) (2020) 20190861, http://dx.doi.org/10.1098/rspa.2019.0861.

[21] F.V. Senhora, O. Giraldo-Londoño, I.F.M. Menezes, G.H. Paulino, Topology optimization with local stress constraints: a stress aggregation-free approach, Struct. Multidiscip. Optim. 62 (2020) 1639–1668, http://dx.doi.org/10.1007/s00158-020-02573-9.

[22] G.A. da Silva, N. Aage, A.T. Beck, O. Sigmund, Local versus global stress constraint strategies in topology optimization: A comparative study, Internat. J. Numer. Methods Engrg. 122 (21) (2021) 6003–6036, http://dx.doi.org/10.1002/nme.6781.

[23] R.D. Kundu, W. Li, X.S. Zhang, Multimaterial stress-constrained topology optimization with multiple distinct yield criteria, Extrem. Mech. Lett. 54 (2022) 101716, http://dx.doi.org/10.1016/j.eml.2022.101716.

[24] J. Yvonnet, D. Da, Topology optimization to fracture resistance: a review and recent developments, Arch. Comput. Methods Eng. 31 (2024) 2295–2315, http://dx.doi.org/10.1007/s11831-023-10044-9.

[25] K. Maute, S. Schwarz, E. Ramm, Adaptive topology optimization of elastoplastic structures, Struct. Optim. 15 (1998) 81–91, http://dx.doi.org/10.1007/BF01278493.

[26] Y. Jia, W. Li, X.S. Zhang, Multimaterial topology optimization of elastoplastic composite structures, J. Mech. Phys. Solids 196 (2025) 106018, http://dx.doi.org/10.1016/j.jmps.2024.106018.

[27] P. Duysinx, M.P. Bendsøe, Topology optimization of continuum structures with local stress constraints, Internat. J. Numer. Methods Engrg. 43 (8) (1998) 1453–1478, http://dx.doi.org/10.1002/(sici)1097-0207(19981230)43:8<1453::aid-nme480>3.0.co;2-2.

[28] E.A. Fancello, J.T. Pereira, Structural topology optimization considering material failure constraints and multiple load conditions, Lat. Am. J. Solids Struct. 1 (1) (2003) 3–24.

[29] C. Le, J. Norato, T. Bruns, C. Ha, D. Tortorelli, Stress-based topology optimization for continua, Struct. Multidiscip. Optim. 41 (2010) 605–620, http://dx.doi.org/10.1007/s00158-009-0440-y.

[30] Y. Luo, Z. Kang, Topology optimization of continuum structures with Drucker–Prager yield stress constraints, Comput. Struct. 90–91 (2012) 65–75, http://dx.doi.org/10.1016/j.compstruc.2011.10.008.

[31] S. Chu, L. Gao, M. Xiao, Z. Luo, H. Li, Stress-based multi-material topology optimization of compliant mechanisms, Internat. J. Numer. Methods Engrg. 113 (7) (2018) 1021–1044, http://dx.doi.org/10.1002/nme.5697.
[32] H. Lian, A.N. Christiansen, D.A. Tortorelli, O. Sigmund, N. Aage, Combined shape and topology optimization for minimization of maximal von Mises stress, Struct. Multidiscip. Optim. 55 (2017) 1541–1557, http://dx.doi.org/10.1007/s00158-017-1656-x.
[33] H. Emmendoerfer, E.A. Fancello, Topology optimization with local stress constraint based on level set evolution via reaction–diffusion, Comput. Methods Appl. Mech. Engrg. 305 (2016) 62–88, http://dx.doi.org/10.1016/j.cma.2016.02.024.
[34] C.-J. Thore, E. Holmberg, A. Klarbring, A general framework for robust topology optimization under load-uncertainty including stress constraints, Comput. Methods Appl. Mech. Engrg. 319 (2017) 1–18, http://dx.doi.org/10.1016/j.cma.2017.02.015.
[35] A. de Assis Pereira, E.L. Cardoso, On the influence of local and global stress constraint and filtering radius on the design of hinge-free compliant mechanisms, Struct. Multidiscip. Optim. 58 (2018) 641–655, http://dx.doi.org/10.1007/s00158-018-1915-5.
[36] D. Da, W. Chen, Simple strategy toward tailoring fracture properties of brittle architected materials, Internat. J. Numer. Methods Engrg. 124 (2) (2023) 334–357, http://dx.doi.org/10.1002/nme.7123.
[37] C. Wang, Y. Wu, Toward static and transient stress-constrained topology optimization for Shell-Infill structures, Comput. Struct. 299 (2024) 107370, http://dx.doi.org/10.1016/j.compstruc.2024.107370.
[38] D. Wei, G. Zhu, Z. Shi, L. Gao, B. Sun, J. Gao, Isogeometric topology optimization for infill designs of porous structures with stress minimization in additive manufacturing, Internat. J. Numer. Methods Engrg. 125 (3) (2024) e7391, http://dx.doi.org/10.1002/nme.7391.
[39] X. Zhang, Z. Ni, A. Takezawa, Y. Wang, Z. Kang, Microscopic stress-constrained two-scale topology optimisation for additive manufacturing, Virtual Phys. Prototyp. 20 (1) (2025) e2450276, http://dx.doi.org/10.1080/17452759.2025.2450276.
[40] W. Ding, H. Liao, X. Yuan, Multi-material topology optimization considering arbitrary strength and yield criteria constraints with single-variable interpolation, Internat. J. Numer. Methods Engrg. 125 (19) (2024) e7561, http://dx.doi.org/10.1002/nme.7561.
[41] Y. Feng, T. Yamada, An assemblable interlocking joint generation method for multi-material topology optimization using interfacial partial stress constraints and dimensional constraints, Comput. Methods Appl. Mech. Engrg. 433 (2025) 117475, http://dx.doi.org/10.1016/j.cma.2024.117475.
[42] Y. Chen, E. Monteiro, I. Koutiri, V. Favier, Stress-constrained topology optimization using the constrained natural element method, Struct. Multidiscip. Optim. 67 (2024) 65, http://dx.doi.org/10.1007/s00158-024-03786-y.
[43] C. Wang, W. Zhang, Finite-life fatigue constrained topology optimization for self-supporting structures in additive manufacturing, Comput. Methods Appl. Mech. Engrg. 436 (2025) 117728, http://dx.doi.org/10.1016/j.cma.2024.117728.
[44] Z. Meng, Q. Qian, P. Hao, On the use of fidelity transformation method for stress-constrained reliability-based topology optimization of continuum structure with high accuracy, Internat. J. Numer. Methods Engrg. 126 (1) (2025) e7602, http://dx.doi.org/10.1002/nme.7602.
[45] D. Da, J. Yvonnet, L. Xia, G. Li, Topology optimization of particle-matrix composites for optimal fracture resistance taking into account interfacial damage, Internat. J. Numer. Methods Engrg. 115 (5) (2018) 604–626, http://dx.doi.org/10.1002/nme.5818.
[46] J.B. Russ, H. Waisman, A novel topology optimization formulation for enhancing fracture resistance with a single quasi-brittle material, Internat. J. Numer. Methods Engrg. 121 (13) (2020) 2827–2856, http://dx.doi.org/10.1002/nme.6334.
[47] C. Wu, J. Fang, S. Zhou, Z. Zhang, G. Sun, G.P. Steven, Q. Li, Level-set topology optimization for maximizing fracture resistance of brittle materials using phase-field fracture model, Internat. J. Numer. Methods Engrg. 121 (13) (2020) 2929–2945, http://dx.doi.org/10.1002/nme.6340.
[48] P. Li, Y. Wu, J. Yvonnet, A SIMP-phase field topology optimization framework to maximize quasi-brittle fracture resistance of 2D and 3D composites, Theor. Appl. Fract. Mech. 114 (2021) 102919, http://dx.doi.org/10.1016/j.tafmec.2021.102919.
[49] J. Desai, G. Allaire, F. Jouve, Topology optimization of structures undergoing brittle fracture, J. Comput. Phys. 458 (2022) 111048, http://dx.doi.org/10.1016/j.jcp.2022.111048.
[50] W. Qiu, Q. Wang, L. Xia, Z. Xia, Designing brittle Fracture-Resistant structures:A tensile strain energy-minimized topology optimization, Comput. Methods Appl. Mech. Engrg. 432 (2024) 117329, http://dx.doi.org/10.1016/j.cma.2024.117329.
[51] J. Han, K. Furuta, T. Kondoh, K. Izui, S. Nishiwaki, K. Terada, Topology optimization with a finite strain nonlocal damage model using the continuous adjoint method, Comput. Methods Appl. Mech. Engrg. 432 (2024) 117333, http://dx.doi.org/10.1016/j.cma.2024.117333.
[52] Q. Zhang, Y. Liu, N. Nguyen-Thanh, W. Li, S. Li, K. Zhou, Adaptive topology optimization for enhancing resistance to brittle fracture using the phase field model, Comput. Methods Appl. Mech. Engrg. 431 (2024) 117237, http://dx.doi.org/10.1016/j.cma.2024.117237.
[53] C. Wu, J. Fang, S. Zhou, Z. Zhang, G. Sun, G.P. Steven, Q. Li, A path-dependent level set topology optimization with fracture criterion, Comput. Struct. 249 (2021) 106515, http://dx.doi.org/10.1016/j.compstruc.2021.106515.
[54] D. Da, X. Qian, Fracture resistance design through biomimicry and topology optimization, Extrem. Mech. Lett. 40 (2020) 100890, http://dx.doi.org/10.1016/j.eml.2020.100890.
[55] B. Bourdin, G. Francfort, J.-J. Marigo, Numerical experiments in revisited brittle fracture, J. Mech. Phys. Solids 48 (4) (2000) 797–826, http://dx.doi.org/10.1016/S0022-5096(99)00028-9.
[56] A. Kumar, B. Bourdin, G.A. Francfort, O. Lopez-Pamies, Revisiting nucleation in the phase-field approach to brittle fracture, J. Mech. Phys. Solids 142 (2020) 104027, http://dx.doi.org/10.1016/j.jmps.2020.104027.
[57] G. Francfort, J.-J. Marigo, Revisiting brittle fracture as an energy minimization problem, J. Mech. Phys. Solids 46 (8) (1998) 1319–1342, http://dx.doi.org/10.1016/S0022-5096(98)00034-9.
[58] A.A. Griffith, VI. The phenomena of rupture and flow in solids, Philos. Trans. R. Soc. Lond. Ser. A Contain. Pap. Math. Phys. Charact. 221 (1921) 163–198, http://dx.doi.org/10.1098/rsta.1921.0006.
[59] Y. Huang, S. Yao, X. Chen, Stress-related topology optimization based on Isogeometric Analysis and global stress measures, Finite Elem. Anal. Des. 245 (2025) 104317, http://dx.doi.org/10.1016/j.finel.2025.104317.
[60] X. Huang, W. Li, K. Nabaki, X. Yan, Reformulation for stress topology optimization of continuum structures by floating projection, Comput. Methods Appl. Mech. Engrg. 423 (2024) 116870, http://dx.doi.org/10.1016/j.cma.2024.116870.
[61] W. Cheng, X. Zhang, T. Hu, J. Li, Y. Wang, Stress-constrained topology optimization using the velocity field level set method, Comput. Struct. 305 (2024) 107577, http://dx.doi.org/10.1016/j.compstruc.2024.107577.
[62] O. Amir, Stress-constrained continuum topology optimization: A new approach based on elasto-plasticity, Struct. Multidiscip. Optim. 55 (2017) 1797–1818, http://dx.doi.org/10.1007/s00158-016-1618-8.
[63] Z. Lei, Y. Liang, G. Cheng, D. Yang, G. Chen, Stress-related discrete variable topology optimization with handling non-physical stress concentrations, Comput. Methods Appl. Mech. Engrg. 431 (2024) 117293, http://dx.doi.org/10.1016/j.cma.2024.117293.
[64] M. Kato, T. Kii, K. Yaji, K. Fujita, Maximum stress minimization via data-driven multifidelity topology design, J. Mech. Des. 147 (8) (2025) 081702, http://dx.doi.org/10.1115/1.4067750.
[65] H. Liao, X. Yuan, R. Gao, An exact penalty function optimization method and its application in stress constrained topology optimization and scenario based reliability design problems, Appl. Math. Model. 125 (2024) 260–292, http://dx.doi.org/10.1016/j.apm.2023.10.014.
[66] J.T. Pereira, E.A. Fancello, C.S. Barcellos, Topology optimization of continuum structures with material failure constraints, Struct. Multidiscip. Optim. 26 (2004) 50–66, http://dx.doi.org/10.1007/s00158-003-0301-z.
[67] G.A. da Silva, N. Aage, A.T. Beck, O. Sigmund, Three-dimensional manufacturing tolerant topology optimization with hundreds of millions of local stress constraints, Internat. J. Numer. Methods Engrg. 122 (2) (2021) 548–578, http://dx.doi.org/10.1002/nme.6548.

[68] M. Kranz, J.K. Lüdeker, B. Kriegesmann, An empirical study on stress-based fail-safe topology optimization and multiple load path design, Struct. Multidiscip. Optim. 64 (2021) 2113–2134, http://dx.doi.org/10.1007/s00158-021-02969-1.
[69] G.A. da Silva, A.T. Beck, O. Sigmund, Structural topology optimization with predetermined breaking points, Comput. Methods Appl. Mech. Engrg. 400 (2022) 115610, http://dx.doi.org/10.1016/j.cma.2022.115610.
[70] G.A. da Silva, H. Emmendoerfer, Fail-safe stress-constrained manufacturing error tolerant topology optimization, Comput. Methods Appl. Mech. Engrg. 421 (2024) 116817, http://dx.doi.org/10.1016/j.cma.2024.116817.
[71] A. Kumar, K. Ravi-Chandar, O. Lopez-Pamies, The revisited phase-field approach to brittle fracture: application to indentation and notch problems, Int. J. Fract. 237 (2022) 83–100, http://dx.doi.org/10.1007/s10704-022-00653-z.
[72] A. Kumar, Y. Liu, J.E. Dolbow, O. Lopez-Pamies, The strength of the Brazilian fracture test, J. Mech. Phys. Solids 182 (2024) 105473, http://dx.doi.org/10.1016/j.jmps.2023.105473.
[73] T.J.R. Hughes, The Finite Element Method: Linear Static and Dynamic Finite Element Analysis, Courier Corporation, 2003.
[74] F. Kamarei, A. Kumar, O. Lopez-Pamies, The poker-chip experiments of synthetic elastomers explained, J. Mech. Phys. Solids 188 (2024) 105683, http://dx.doi.org/10.1016/j.jmps.2024.105683.
[75] O. Lopez-Pamies, J.E. Dolbow, G.A. Francfort, C.J. Larsen, Classical variational phase-field models cannot predict fracture nucleation, Comput. Methods Appl. Mech. Engrg. 433 (2025) 117520, http://dx.doi.org/10.1016/j.cma.2024.117520.
[76] A. Kumar, G.A. Francfort, O. Lopez-Pamies, Fracture and healing of elastomers: A phase-transition theory and numerical implementation, J. Mech. Phys. Solids 112 (2018) 523–551, http://dx.doi.org/10.1016/j.jmps.2018.01.003.
[77] D.C. Drucker, W. Prager, Soil mechanics and plastic analysis or limit design, Quart. Appl. Math. 10 (2) (1952) 157–165, http://dx.doi.org/10.1090/qam/48291.
[78] D. Munz, T. Fett, Ceramics: Mechanical Properties, Failure Behaviour, Materials Selection, Springer Science & Business Media, 2013.
[79] E. Tanné, T. Li, B. Bourdin, J.J. Marigo, C. Maurini, Crack nucleation in variational phase-field models of brittle fracture, J. Mech. Phys. Solids 110 (2018) 80–99, http://dx.doi.org/10.1016/j.jmps.2017.09.006.
[80] H. Tada, P.C. Paris, G.R. Irwin, The Stress Analysis of Cracks, Handbook, Del Research Corporation, 1973.
[81] B. Bourdin, Filters in topology optimization, Internat. J. Numer. Methods Engrg. 50 (9) (2001) 2143–2158, http://dx.doi.org/10.1002/nme.116.
[82] F. Wang, B.S. Lazarov, O. Sigmund, On projection methods, convergence and robust formulations in topology optimization, Struct. Multidiscip. Optim. 43 (2011) 767–784, http://dx.doi.org/10.1007/s00158-010-0602-y.
[83] G.A. da Silva, A.T. Beck, O. Sigmund, Stress-constrained topology optimization considering uniform manufacturing uncertainties, Comput. Methods Appl. Mech. Engrg. 344 (2019) 512–537, http://dx.doi.org/10.1016/j.cma.2018.10.020.
[84] C. Wang, Z. Zhao, X.S. Zhang, Inverse design of magneto-active metasurfaces and robots: Theory, computation, and experimental validation, Comput. Methods Appl. Mech. Engrg. 413 (2023) 116065, http://dx.doi.org/10.1016/j.cma.2023.116065.
[85] Y. Saad, M.H. Schultz, GMRES: A generalized minimal residual algorithm for solving nonsymmetric linear systems, SIAM J. Sci. Stat. Comput. 7 (3) (1986) 856–869, http://dx.doi.org/10.1137/0907058.
[86] K. Svanberg, The method of moving asymptotes—a new method for structural optimization, Internat. J. Numer. Methods Engrg. 24 (2) (1987) 359–373, http://dx.doi.org/10.1002/nme.1620240207.
[87] Y. Jia, C. Wang, X.S. Zhang, FEniTop: A simple FEniCSx implementation for 2D and 3D topology optimization supporting parallel computing, Struct. Multidiscip. Optim. 67 (2024) 140, http://dx.doi.org/10.1007/s00158-024-03818-7.
[88] I.A. Baratta, J.P. Dean, J.S. Dokken, M. Habera, J.S. Hale, C.N. Richardson, M.E. Rognes, M.W. Scroggs, N. Sime, G.N. Wells, DOLFINx: The next generation FEniCS problem solving environment, 2023, http://dx.doi.org/10.5281/zenodo.10447666.
[89] Y. Liu, O. Lopez-Pamies, J.E. Dolbow, On the effects of material strength in dynamic fracture: A phase-field study, 2024, http://dx.doi.org/10.48550/arXiv.2411.16393, arXiv:2411.16393.
[90] Z. Zhao, X.S. Zhang, Design of graded porous bone-like structures via a multi-material topology optimization approach, Struct. Multidiscip. Optim. 64 (2021) 677–698, http://dx.doi.org/10.1007/s00158-021-02870-x.
[91] R.D. Kundu, X.S. Zhang, Stress-based topology optimization for fiber composites with improved stiffness and strength: Integrating anisotropic and isotropic materials, Compos. Struct. 320 (2023) 117041, http://dx.doi.org/10.1016/j.compstruct.2023.117041.
[92] N. Noii, H.A. Jahangiry, H. Waisman, Level-set topology optimization for ductile and brittle fracture resistance using the phase-field method, Comput. Methods Appl. Mech. Engrg. 409 (2023) 115963, http://dx.doi.org/10.1016/j.cma.2023.115963.
[93] Y. Jia, X.S. Zhang, Multimaterial topology optimization for finite strain elastoplasticity: theory, methods, and applications, 2025, http://dx.doi.org/10.48550/arXiv.2502.02052, arXiv:2502.02052.
[94] O. Giraldo-Londoño, G.H. Paulino, PolyStress: a Matlab implementation for local stress-constrained topology optimization using the augmented Lagrangian method, Struct. Multidiscip. Optim. 63 (2021) 2065–2097, http://dx.doi.org/10.1007/s00158-020-02760-8.
[95] A. Klarbring, N. Strömberg, Topology optimization of hyperelastic bodies including non-zero prescribed displacements, Struct. Multidiscip. Optim. 47 (2013) 37–48, http://dx.doi.org/10.1007/s00158-012-0819-z.
[96] R. Bharali, S. Goswami, C. Anitescu, T. Rabczuk, A robust monolithic solver for phase-field fracture integrated with fracture energy based arc-length method and under-relaxation, Comput. Methods Appl. Mech. Engrg. 394 (2022) 114927, http://dx.doi.org/10.1016/j.cma.2022.114927.
[97] A. Gupta, U.M. Krishnan, T.K. Mandal, R. Chowdhury, V.P. Nguyen, An adaptive mesh refinement algorithm for phase-field fracture models: Application to brittle, cohesive, and dynamic fracture, Comput. Methods Appl. Mech. Engrg. 399 (2022) 115347, http://dx.doi.org/10.1016/j.cma.2022.115347.